Monthly Notices
of the
ROYAL ASTRONOMICAL SOCIETY

MNRAS **480,** 3993–4016 (2018)
Advance Access publication 2018 August 3

doi:10.1093/mnras/sty2113

# Direct evidence of AGN feedback: a post-starburst galaxy stripped of its gas by AGN-driven winds

Dalya Baron,[1]★ Hagai Netzer,[1] J. Xavier Prochaska,[2] Zheng Cai,[2] Sebastiano Cantalupo,[3] D. Christopher Martin,[4] Mateusz Matuszewski,[4] Anna M. Moore,[5] Patrick Morrissey[4] and James D. Neill[4]

[1]*School of Physics and Astronomy, Tel-Aviv University, Tel Aviv 69978, Israel*
[2]*Department of Astronomy and Astrophysics, UCO/Lick Observatory, University of California, 1156 High Street, Santa Cruz, CA 95064, USA*
[3]*Department of Physics, ETH Zurich, Wolfgang-Pauli-Strasse 27, CH-8093 Zurich, Switzerland*
[4]*California Institute of Technology, 1216 East California Boulevard, Pasadena, CA 91125, USA*
[5]*Research School of Astronomy and Astrophysics, Australian National University, Canberra, ACT 2611, Australia*

Accepted 2018 August 1. Received 2018 June 26; in original form 2018 March 25

## ABSTRACT

Post-starburst E+A galaxies show indications of a powerful starburst that was quenched abruptly. Their disturbed, bulge-dominated morphologies suggest that they are merger remnants. The more massive E+A galaxies are suggested to be quenched by active galactic nucleus (AGN) feedback, yet little is known about AGN-driven winds in this short-lived phase. We present spatially resolved integral field unit spectroscopy by the Keck Cosmic Web Imager of SDSS J003443.68 + 251020.9, at $z = 0.118$. The system consists of two galaxies, the larger of which is a post-starburst E+A galaxy hosting an AGN. Our modelling suggests a 400 Myr starburst, with a peak star formation rate of 120 $M_\odot$ yr$^{-1}$. The observations reveal stationary and outflowing gas, photoionized by the central AGN. We detect gas outflows to a distance of 17 kpc from the central galaxy, far beyond the region of the stars (∼3 kpc), inside a conic structure with an opening angle of 70 deg. We construct self-consistent photoionization and dynamical models for the different gas components and show that the gas outside the galaxy forms a continuous flow, with a mass outflow rate of about 24 $M_\odot$ yr$^{-1}$. The gas mass in the flow, roughly $10^9$ $M_\odot$, is larger than the total gas mass within the galaxy, some of which is outflowing too. The continuity of the flow puts a lower limit of 60 Myr on the duration of the AGN feedback. Such AGNs are capable of removing, in a single episode, most of the gas from their host galaxies and expelling enriched material into the surrounding circumgalactic medium.

**Key words:** galaxies: active – galaxies: evolution – galaxies: general – galaxies: interactions – galaxies: star formation.

## 1 INTRODUCTION

The discovery of a strong correlation between the masses of supermassive black holes (SMBHs) and the velocity dispersions and bulge mass of their host galaxies (Gebhardt et al. 2000; Ferrarese & Merritt 2000; Tremaine et al. 2002; Gültekin et al. 2009) led to various suggestions about the connection between SMBH growth and stellar mass growth in galaxies, in particular the quenching of star formation (SF) due to BH activity. Such feedback is now a key ingredient in galaxy formation theories (Silk & Rees 1998; Springel et al. 2005; Springel, Di Matteo & Hernquist 2005; Hopkins et al. 2006). Several such models include a scenario in which an active galactic nucleus (AGN) drives galactic-scale winds that expel gas from its host galaxy, shuts down additional gas accretion onto the SMBH, terminates the SF in the galaxy, and enriches its circumgalactic medium (CGM) with metals (Silk & Rees 1998; Fabian 1999; Benson et al. 2003; King 2003; Di Matteo, Springel & Hernquist 2005; Hopkins et al. 2006; Gaspari et al. 2011).

AGN-driven winds are ubiquitous and span a large range of host galaxy properties. They are observed in systems at different evolutionary stages, with a large range of star formation rates (SFRs): from ultraluminous infrared galaxies (ULIRGs, Rupke, Veilleux & Sanders 2005; Rupke & Veilleux 2013; Spoon et al. 2013; Veilleux et al. 2013; Rodríguez Zaurín et al. 2013; Sun et al. 2014; García-Burillo et al. 2015; Fiore et al. 2017), which show powerful star-

★ E-mail: dalyabaron@mail.tau.ac.il

© 2018 The Author(s)
Published by Oxford University Press on behalf of the Royal Astronomical Society

Downloaded from https://academic.oup.com/mnras/article-abstract/480/3/3993/5066189 by California Institute of Technology user on 28 November 2018

bursts, to quenched elliptical galaxies (e.g. Cheung et al. 2016). They are detected on different physical scales, from the vicinity of the SMBH (few gravitational radii; Blustin et al. 2003; Reeves, O'Brien & Ward 2003; Tombesi et al. 2010) to galactic scales (∼1–10 kpc, e.g. Greene et al. 2011; Cano-Díaz et al. 2012; Liu et al. 2013a,b; Harrison et al. 2014; Rupke, Gültekin & Veilleux 2017). They are traced via different gas-phase indicators related to different ionization states – from high velocity X-ray and ultraviolet (UV) absorption lines (e.g. Blustin et al. 2003; Reeves et al. 2003; Tombesi et al. 2010; Arav et al. 2013), through ionized emission lines (Greene et al. 2011; Cano-Díaz et al. 2012; Harrison et al. 2014; Zakamska et al. 2016; Rupke et al. 2017), to atomic and molecular emission and absorption lines (Feruglio et al. 2010; Veilleux et al. 2013; Cicone et al. 2014; García-Burillo et al. 2015; Rupke et al. 2017). While outflows are detected in both type I and type II AGNs (Heckman et al. 1981; Feldman et al. 1982; Heckman, Miley & Green 1984; Greene & Ho 2005; Nesvadba et al. 2006; Moe et al. 2009; Rosario et al. 2010; Greene et al. 2011; Cano-Díaz et al. 2012; Arav et al. 2013; Mullaney et al. 2013; Zakamska et al. 2016; Fiore et al. 2017), it is still unclear whether such winds are capable of expelling a large enough mass of gas from their host galaxies to significantly affect their evolution. Furthermore, there are very few systems in which this scenario was observed in action, i.e. systems in which most of the gas was recently driven out of the galaxy (see examples of possible candidates in Greene et al. 2011; Liu et al. 2013b; Sun et al. 2018). At high redshift of $z \approx 2$, Cai et al. (2017) identified a $\gtrsim 30$ kpc extended C IV and He II emission in the radio-quiet MAMMOTH-1 enormous nebula, which they interpret as a direct evidence of an AGN outflow at high redshift.

A major uncertainty concerning galactic-scale feedback is the relative contribution of AGN-driven versus supernovae (SNe)-driven winds, where the latter is directly related to SF activity in the galaxy. The current largest samples of observed outflows come from optical surveys, such as the Sloan Digital Sky Survey (SDSS) (York et al. 2000), where blueshifted and asymmetric emission lines are used to select systems with winds (see e.g. Mullaney et al. 2013). In most of these samples, only the [O III]λ5007Å emission line shows a blueshifted profile, which is not enough to determine the ionization source of the winds (SF, AGN, or shocks). Studies either focus on type I AGN, where the accretion disc (AD) is detected directly, or use narrow emission-line diagnostics (see e.g. Kewley et al. 2006) to select systems in which there is an obscured type II AGN. Although the AGN is the main ionizing source of the stationary (and sometimes the outflowing) gas, in all such sources, it is unclear whether it is also the main driver of the observed winds. This is due to the fact that most systems showing AGN activity also show significant SF activity, with some correlation between the AGN bolometric luminosity and the SF luminosity (e.g. Netzer 2009). Many systems with more powerful AGN, that are capable of producing stronger AGN-driven winds, also undergo powerful SF episodes, capable of driving stronger SNe-driven winds.

A similar uncertainty is associated with pure SF galaxies selected by line-diagnostic diagrams (see a comprehensive study by Cicone, Maiolino & Marconi 2016). These systems do not show evidence of current AGN activity, but due to the relatively short AGN duty cycle it is not clear whether the AGN was active in the recent past and might have contributed to the currently observed winds. Thus, the time-scale of the observed winds, and the relation to AGN and/or SF activity, are crucial for the understanding of the various types of feedback. As explained below, we suggest that detailed integral field unit (IFU) observations of relatively nearby post-starburst galaxies can help to answer such questions.

Post-starburst E+A galaxies (also called H$\delta$-strong and K+A galaxies) offer an advantage over other galaxy samples in dealing with these uncertainties (Wild, Heckman & Charlot 2010). These systems show prominent Balmer absorption lines in their optical spectra, and no contribution from O- and B-type stars (Dressler et al. 1999; Poggianti et al. 1999; Goto 2004; Dressler et al. 2004). Their spectrum indicates a recent starburst that was quenched abruptly, with a narrow stellar age distribution, completely dominated by intermediate-age stars (typically A-type stars). The estimated SFRs during the burst range from 50 to 300 $M_{\odot}yr^{-1}$ (Poggianti & Wu 2000; Kaviraj et al. 2007), and the mass fractions forming in the burst are high, 30 per cent–80 per cent of the total stellar mass (Liu & Green 1996; Bressan, Poggianti & Franceschini 2001; Norton et al. 2001; Yang et al. 2004; Kaviraj et al. 2007). Many of these systems show bulge-dominated morphologies, with tidal features or close companions, which suggest a late-stage merger (Canalizo et al. 2000; Yang et al. 2004; Goto 2004; Cales et al. 2011). Due to the short lifetime of A-type stars, this evolutionary stage must be very short, making such systems a small fraction of the total galaxy population (Goto et al. 2003; Goto 2007; Wild et al. 2009; Yesuf et al. 2014; Alatalo et al. 2016a).

Various studies suggest that post-starburst E+A galaxies are the evolutionary link between gas-rich major mergers (ULRIGs) and quiescent, early-type, galaxies (Yang et al. 2004, 2006; Kaviraj et al. 2007; Wild et al. 2009; Cales et al. 2011, 2013; Yesuf et al. 2014; Cales & Brotherton 2015; French et al. 2015; Alatalo et al. 2016a,b; Wild et al. 2016; Baron et al. 2017). According to this scenario, a gas-rich major merger triggers a powerful starburst, and gas is funnelled to the vicinity of the SMBH, triggering an AGN. Soon after, the AGN launches nuclear winds which sweep-up the gas in the galaxy, shutting down the current starburst abruptly, and removing the gas from the host galaxy (Kaviraj et al. 2007; Cales et al. 2013; Cales & Brotherton 2015). The system is observed as a post-starburst E+A galaxy, which soon becomes a quiescent elliptical galaxy. Kaviraj et al. (2007) performed the first comprehensive observational and theoretical study of the quenching process that terminates the starburst in E+A galaxies. They found a bimodal behaviour, where in galaxies less massive than $M = 10^{10}$ $M_{\odot}$, SN-driven feedback is the main quenching mechanism, while galaxies above this mass are mainly quenched by an AGN (see also Li et al. 2018). They suggested, based on calculated star formation histories (SFHs), that the latter were indeed ULIRGs. According to this scenario, one may expect to detect galactic-scale AGN-driven winds in these systems.

For E+A galaxies with an active BH and ongoing observed winds, it is clear that the observed outflows are driven solely by the AGN, since the starburst is fully quenched. This allows the study of wind properties and dynamics in the context of pure AGN feedback. Furthermore, since the stellar age throughout the entire galaxy is dominated by a single, short, starburst episode, it allows a comparison between winds observed in different systems as a function of time since the onset (or termination) of the burst (Wild et al. 2010). The comparison of several similar systems of this type can serve as a well-defined timeline that provide the necessary missing details for AGN feedback in this phase.

In recent years, studies using optical and NIR IFUs have provided detailed information about spatially resolved outflows that are traced by ionized gas (Greene et al. 2011; Cano-Díaz et al. 2012; Liu et al. 2013a,b; Harrison et al. 2014; Rupke et al. 2017). However, observations of high-redshift systems of this type cannot resolve scales below several kpc and in low-redshift systems, there is confusion about the source of the observed winds with contribu-



Downloaded from https://academic.oup.com/mnras/article-abstract/480/3/3993/5066189 by California Institute of Technology user on 28 November 2018

tions from both AGN and stellar radiation fields (e.g. Harrison et al. 2014). It is essential to improve the observations and modelling of the nearby systems and also focus on a well-defined sample of objects (starburst galaxies, post-starburst galaxies, mergers, etc.), since feedback can take different forms, depending on the morphology of the system and its (usually undetermined) age. This work, which is the second in a series of papers on feedback in E+A galaxies, provides many of the missing details for one such system, using optical IFU observations.

We have recently detected the first evidence of an AGN-driven outflow, traced by ionized gas, in a post-starburst E+A galaxy (Baron et al. 2017; see also Tremonti, Moustakas & Diamond-Stanic 2007, Tripp et al. 2011, and Yesuf et al. 2017). SDSS J132401.63+454620.6 was discovered as an outlier by the anomaly detection algorithm of Baron & Poznanski (2017), and our ESI/Keck spectroscopy revealed a post-starburst system with powerful ionized outflows. We measured the mass outflow rate in this system to be in the range 4–120 $M_{\odot}yr^{-1}$, similar to outflows observed in ULIRGs. Since then, we have constructed a sample of such galaxies, with fully quenched starbursts and powerful AGN-driven winds. In this work, we present spatially resolved spectroscopy, obtained by the Keck Cosmic Web Imager (KCWI), of a second E+A galaxy at $z = 0.118$, SDSS J003443.68+251020.9. Our observations reveal ionized winds that extend far beyond the host galaxy, with most of the gas mass already detached from the main stellar mass. We describe the observations in Section 2, and discuss the general observed properties of the system in Section 3. We then construct a photoionization and dynamical model for the system in Section 4, and measure masses and mass outflow rates in Section 4.7. We discuss our finding in Section 5 and conclude in Section 6. Throughout this paper, we assume a cosmology with $\Omega_M = 0.3$, $\Omega_\Lambda = 0.7$, and $h = 0.7$, thus 1 arcsec corresponds to 2.1 kpc for the system in question.

## 2 OBSERVATIONS

### 2.1 1D spectroscopy from SDSS

SDSS J003443.68+251020.9 was observed as part of the general SDSS survey (York et al. 2000). The spectrum was obtained using the BOSS spectrograph with a 2 arcsec fibre, which covers a wavelength range of 3800–9200Å, with a resolving power going from 1560 at 3700 Å to 2650 at 9000 Å, resulting in a spectral resolution of 190 and 110 km $s^{-1}$ respectively. The publicly available spectrum of the galaxy is combined from three 15 m sub-exposures, and with signal-to-noise ratios (S/N) ranging from 10 to 25. We did not find spectral differences between the three sub-exposures. The image of the galaxy was taken in the SDSS broad-band filters with a typical seeing of 1–1.2 arcsec.

### 2.2 Spatially resolved spectroscopy with KCWI

The KCWI is a new facility instrument for the Keck II telescope at the W. M. Keck Observatory (WMKO; Martin et al. 2010; Morrissey et al. 2012, 2018). KCWI is a bench-mounted spectrograph installed at the Keck II right Nasmyth focal station, providing integral field spectroscopy over a seeing-limited field of up to 20 arcsec × 33 arcsec in extent, with high efficiency and spectral resolution in the range 1000–20 000. KCWI will provide full wavelength coverage (0.35–1.05 μm) using optimized blue and red channels, with the blue channel (0.35–0.55 μm) currently in operation.

We observed the system on the night of 2017 October 20. Conditions were clear with seeing of approximately 1 arcsec. Observations were carried out with the medium slicer, which gives a 16.5 arcsec × 20.4 arcsec field of view, with a slice width of 0.69 arcsec. We used the BM grating configuration, tilted to provide wavelength coverage of 4600—5700 Å, with a spectral resolution of 0.28 Å. Three exposures of 600 s provided a combined binned data cube, with a median S/N per spatial pixel (spaxel) between 2 and 12 in the regions where a source is detected. The average surface brightness limit of the combined cube is about $1.5 \times 10^{-18}$ erg $s^{-1}cm^{-2}Å^{-1}$ arcsec$^{-2}$.

The standard KCWI pipeline[1] was used to reduce the data (also see brief description in Cai et al. in preparation). For each data cube, the bias was subtracted, the pixel-to-pixel variation was corrected, and the cosmic rays were removed. We corrected the geometric distortion using the continuum bar images. The arc images were used to calibrate the wavelength solution. The slice-to-slice variance was further removed using the twilight flats. We use the BD+28D4211 taken at the beginning of the night to conduct the flux calibration.

In order to subtract sky emission lines, we choose three different off-source regions and bin their spectra. We subtract the binned spectrum from all the spaxels in the cube. Once the sky emission is subtracted, an integration over 2 arcsec around the primary galaxy gives a spectrum that is similar to that by the SDSS. Like SDSS, vacuum wavelength are used for all observations.

## 3 GENERAL OBSERVED PROPERTIES

In Fig. 1, we show the SDSS *gri* colour-composite image of the system. The system is composed of two galaxies, which we refer to as the primary and the companion. An SDSS spectrum is available only for the primary galaxy. We study the stellar properties of the primary in Section 3.1, and provide details about the companion in Section 3.2. The properties of the AGN and the gas in the system are described in Section 3.3. Throughout the section, we use both SDSS and KCWI data. While KCWI data are superior in terms of its spectral resolution, spatial resolution, and S/N, it covers a limited wavelength range compared to the SDSS spectrum. The SDSS spectrum is an integration through a 2 arcsec fibre around the centre of the primary galaxy. We refer to it throughout the section as the 'global spectrum'.

### 3.1 The primary galaxy

The SDSS colour-composite image (Fig. 1) shows that the primary galaxy has a bulge-dominated morphology, with a nearby companion, and additional diffuse emission around the two systems. Thus, we most likely observe a galaxy interaction. We fit a Sérsic profile to the primary images in the *g* and *r* bands and find Sérsic indices of 4.9 and 4.1, respectively. These values are subject to large uncertainties since the seeing during the observation (1 arcsec) is of the order of the size of the primary galaxy. Therefore, given the data, we cannot distinguish between a Sérsic index of 4.9 and a de Vaucouleurs profile.

In Fig. 2, we show the global spectrum of the primary galaxy. The spectrum is dominated by A-type stars and shows strong Balmer absorption lines, the clear signature of post-starburst E+A galaxies.

[1]KCWI pipeline: https://github.com/kcwidev/kderp/blob/master. A forthcoming paper will describe the KCWI pipeline in detail (Neill et al. in preparation).



Downloaded from https://academic.oup.com/mnras/article-abstract/480/3/3993/5066189 by California Institute of Technology user on 28 November 2018

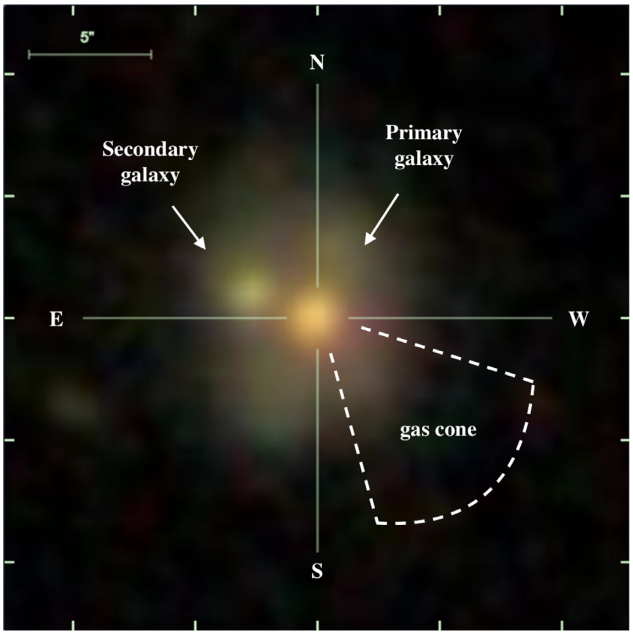


**Figure 1.** The *gri* colour-composite image of SDSS J003443.68+251020.9. The image shows two different galaxies in the field, which we call the primary and secondary galaxies. An SDSS spectrum is available only for the primary galaxy. The white dashed lines mark the region in which we detect ionized gas emission.

The equivalent width (EW) of the H$\delta$ absorption line is 7.8 Å, which is above the 5 Å threshold typically used to select E+A galaxies (see e.g. Goto 2007; Alatalo et al. 2016a). We fitted a stellar population synthesis model to the spectrum using the Penalized Pixel-Fitting stellar kinematics extraction code (PPXF; Cappellari 2012), which is a public code for extracting the stellar kinematics and stellar population from absorption-line spectra of galaxies (Cappellari & Emsellem 2004) . It uses the MILES library, which contains single stellar population synthesis models and covers the full range of the optical spectrum with a resolution of full width at half-maximum (FWHM) of 2.3Å (Vazdekis et al. 2010). The output of the code includes the relative weight of stars with different ages, the stellar velocity dispersion, the dust reddening towards the stars (assuming a Calzetti et al. 2000 extinction law), and the best-fitting stellar model, which we mark with pink in Fig. 2. The diagram also shows (right-hand panel) that the emission lines are blueshifted, by about 150 km s$^{-1}$, relative to the stellar absorption lines that are used to define the systemic velocity of the primary galaxy.

The best-fitting model shows a stellar age distribution which consists of two SF episodes, with a total mass-weighted stellar age of 0.28 Gyr. According to the model, the recent episode, which dominates the spectrum of the galaxy, started 400 Myr ago and ended 200 Myr ago, with peak SFR of 120 M$_\odot$yr$^{-1}$. There is no contribution from O- and B-type stars to the model, which means that there is no ongoing SF in the galaxy. The older SF episode is poorly constrained due to its weak contribution to the spectrum. The age of the older episode is centred around 5 Gyr, with a width of 2 Gyr. However, we find reasonable fits even when forcing the code to use templates with different ages within the range 3–10 Gyr. The dust reddening towards the stars is $E(B-V) = 0.45$ mag, within the range observed in star-forming galaxies (Kauffmann et al. 2003b). The stellar velocity dispersion is 170 km s$^{-1}$, which is well resolved due to the relatively broad absorption lines in A stars. We use the best stellar population synthesis model to measure the stellar mass, which is $\log \mathrm{M}/\mathrm{M}_\odot = 10.8$. We use the KCWI data to show below that the stellar continuum of the primary galaxy is detected to 3 kpc. Therefore, the steepness of the light profile suggests that the fibre-based stellar mass measurement, which covers 4.3 kpc, is a good approximation of the total stellar mass of the system.

### 3.2 The companion galaxy

As noted above, there is no SDSS spectrum for the companion galaxy. In order to study its properties we use the KCWI data, and sum all the spaxels within a 2 arcsec × 2 arcsec region around its centre. The summed spectrum is shown in Fig. 3. We use PPXF to fit stellar population synthesis model to the galaxy, and mark the best fit in Fig. 3 with pink. The best-fitting model shows a good agreement with the summed spectrum. However, a large combination of parameters give practically the same stellar continuum, and given the limited wavelength range we cannot robustly determine the age of the recent burst, its duration, or the dust reddening. The strength of the H$\gamma$ absorption line (EW $\sim$ 10 Å) hints that this could also be a post-starburst system. This can only be confirmed by observations with a larger wavelength coverage.

One can also see in Fig. 3 that the H$\beta$ emission line is almost as strong as [O III]. Therefore, we can rule out Seyfert-type ionization for the gas in the secondary galaxy. Based on the available data, we cannot distinguish between SF or low-ionization nuclear emission-line region (LINER)-like radiation field. We further note that the two galaxies are unresolved in the *WISE* images, therefore we cannot use W1, W2, W3, and W4 as further diagnostics for the source of ionization in this galaxy.

### 3.3 Active black hole and AGN photoionized gas

The spectrum of the primary galaxy is very similar to that studied by Baron et al. (2017), where we found a post-starburst E+A galaxy with AGN. The emission-line spectrum of the primary galaxy is typical of type II (obscured) AGN. The ionized gas can be roughly divided into three components: (1) the narrow-line region (NLR) within the primary galaxy, (2) a broad kinematic component within the primary galaxy, and (3) gas that resides outside the primary galaxy to distances of 17 kpc. We study the gas within the galaxy in Section 3.3.1. We then use the spatially resolved KCWI data to study the gas outside the galaxy in Section 3.3.2.

#### *3.3.1 The NLR and broad outflowing central component*

We subtract the best-fitting stellar model from the global spectrum and obtain the emission-line spectrum of the central gas component. We show six parts of this spectrum in Appendix A (Fig. A1), where we plot [O III] λλ 4959,5007Å, H$\alpha$ λ 6563Å and [N II] λλ 6548,6584Å, [O II] λλ 3725,3727Å and H$\beta$ λ 4861Å, and [O I] λλ 6300,6363Å and [S II] λλ 6717,6731Å (hereafter [O III], H$\alpha$, [N II], [O II], H$\beta$, [O I], and [S II]). The Balmer lines and the forbidden line profiles show narrow as well as broad components. We also detect [Ne III ] λ 3869Å emission, which we do not show in Fig. A1.

The appendix to this paper explains the procedure used to fit the various line profiles. Here, we only refer to the line-diagnostic diagrams based on the fits. The new high spatial and spectral resolution observations presented in Section 3.3.2 are far superior to the SDSS spectrum and hence we defer the more detailed description of the line profile in the different locations to that section.



Downloaded from https://academic.oup.com/mnras/article-abstract/480/3/3993/5066189 by California Institute of Technology user on 28 November 2018

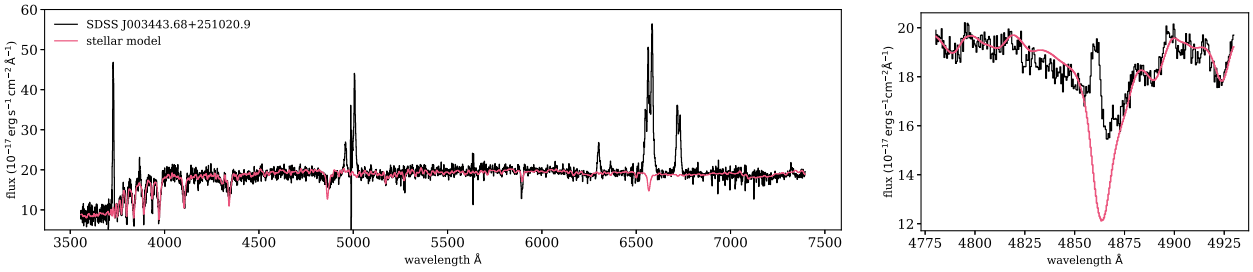


**Figure 2.** Left-hand panel: the SDSS 1D spectrum of SDSS J003443.68+251020.9 (black), and the best population synthesis model (pink) using PPXF. Right-hand panel: zoom-in on the H$\beta$ region of the KCWI spectrum of the primary galaxy, showing that the H$\beta$ emission line is shifted from the systemic velocity, defined by the stellar absorption lines.

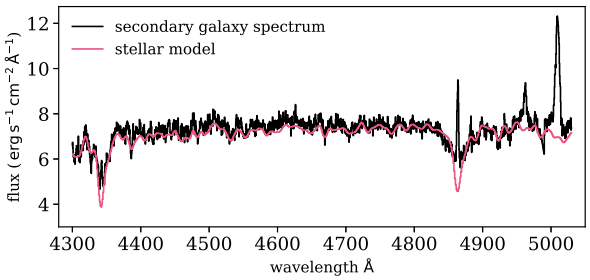


**Figure 3.** The summed KCWI spectrum of the companion galaxy over a region of 2 arcsec × 2 arcsec (black), and the best population synthesis model (pink) using PPXF. Although the wavelength range is limited, the stellar spectrum and its best fit are similar to what we find for the primary galaxy.

In Fig. 4, we show the narrow (blue) and the broad (green) emission components on line-diagnostic diagrams (Baldwin, Phillips & Terlevich 1981; Veilleux & Osterbrock 1987). The left-hand panel shows log [O III ]/H$\beta$ versus log [N II ]/H$\alpha$. We show three separating criteria, the first is a theoretical upper limit which separates starbursts and AGN-dominated galaxies (Ke01; black line Kewley et al. 2001). The second is a modified criterion which includes composite galaxies showing contributions from both SF and AGN (Ka03; grey line, Kauffmann et al. 2003a). We use the criterion by Cid Fernandes et al. (2010) to separate between LINERs and Seyferts (CF10; yellow). The middle and the right-hand panels show log [O III]/H$\beta$ versus log [S II]/H$\alpha$ and log [O I]/H$\alpha$, respectively. We also mark the Kewley et al. (2006) separating line between LINER and Seyfert galaxies (Ke06; pink line). One can see that in all three diagrams both the narrow and the broad components are classified as AGN-dominated. The narrow emission lines are consistent with a LINER-type, low ionization, spectrum while the broad lines are consistent with a Seyfert-like, high ionization, spectrum. We note that all these properties are similar to those we observed in SDSS J132401.63+454620.6, the first post-starburst E+A galaxy analysed using such methods (Baron et al. 2017).

We use the measured H$\alpha$/H$\beta$ flux ratios to derive the global dust reddening towards the two kinematic components. Assuming case-B recombination, a gas temperature of $10^4$ K (Osterbrock & Ferland 2006), a dusty screen, and the Cardelli, Clayton & Mathis (1989) extinction law, the colour excess is given by:

$$E(B-V) = 2.33 \log \left[ \frac{(\mathrm{H}\alpha/\mathrm{H}\beta)_{\mathrm{obs}}}{2.85} \right] \quad (1)$$

where $(\mathrm{H}\alpha/\mathrm{H}\beta)_{\mathrm{obs}}$ is the observed line ratio. Using this relation, we find $E(B-V) = 0.5$ mag for the narrow lines and $E(B-V) = 1.7$ mag for the broad lines. The values differ by less than 10 per cent when using Small Magellanic Cloud or Large Magellanic Cloud extinction curves (e.g. Baron et al. 2016). The dust reddening of the narrow component is similar to the reddening derived for the stars, although the two are derived under different geometric assumptions (the stellar reddening is derived with the Calzetti et al. 2000 law, which is more appropriate for stars). It is also consistent with the dust reddening typically measured for NLR gas in AGN (see, e.g. Kewley et al. 2006). The dust reddening of the broad component is significantly higher, similar to what we found for SDSS J132401.63+454620.6 in Baron et al. (2017). In Section 4.3 below we look into the emission-line reddening in more detail, considering also the case where the dust is mixed with the ionized gas.

### 3.3.2 *Outflowing extended gas*

The KCWI observations cover the rest-frame wavelength range 4200–5120 Å, allowing us to measure the following emission lines: H$\gamma$, He II λ 4686Å, H$\beta$, and the two [O III] lines. The continuum emission, which is due to the stars in the primary and the secondary galaxies, is similar to the SDSS colour composite shown in Fig. 1. Since we are interested in the gas emission throughout the field, we proceed to remove the stellar continuum emission from each individual spaxel. We use PPXF to fit the stellar continuum in each spaxel. Although the wavelength range is limited, manual inspection of the best-fitting templates show good fits to the observed spectra, and similar templates for different spaxels. The latter is partially due to the point spread function (PSF) broadening. We subtract the best-fitting template from each spectrum to obtain the pure emission-line spectrum for each spaxel.

The top two panels of Fig. 5 show the stars and the [O III] emission in the entire system. Stellar light is detected up to a distance of about 3 kpc from the centre of the primary galaxy while gas emission extends, in a conic-shaped structure in the south-west direction, up to a projected distance of about 17 kpc. The other panels of Fig. 5 show the [O III] flux for different velocity channels, compared to the systematic velocity of the stars in the primary galaxy. Each velocity channel covers about 100 km s$^{-1}$ and we sum the observed [O III] in this range. We use a logarithmic colour coding and keep the same dynamical range for all the different panels, where yellow represents high flux and purple represents low flux. We overplot with orange contours the stellar continuum emission, where the largest orange contour represents the region which is consistent with non-detection. The primary galaxy shows [O III] emission with a velocity of 150 km s$^{-1}$ with respect to the stellar population, and the secondary galaxy (located at −5,0 kpc) shows [O III] with a velocity of approximately +200 km s$^{-1}$ with respect to the primary

Downloaded from https://academic.oup.com/mnras/article-abstract/480/3/3993/5066189 by California Institute of Technology user on 28 November 2018

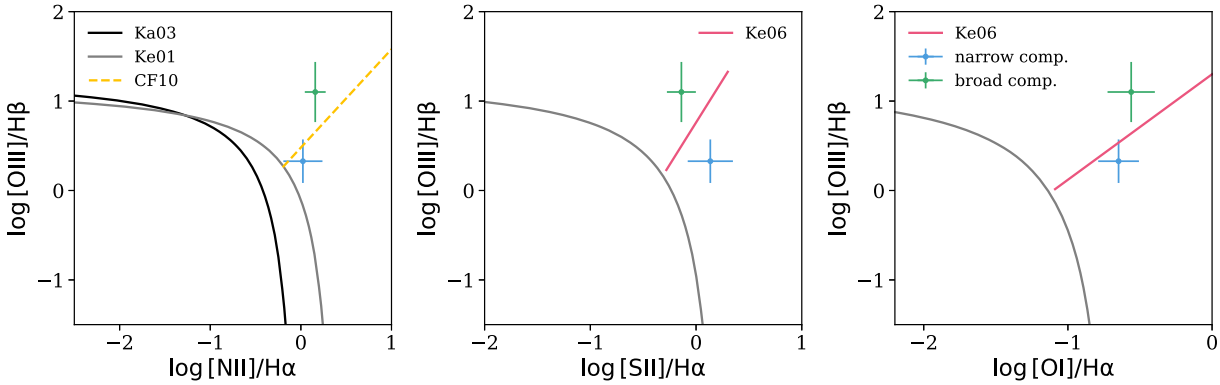


**Figure 4.** Classification diagrams for the narrow (blue) and broad (green) emission lines, as measured from the 2 arcsec SDSS fibre. The left-hand panel shows log [O III]/H$\beta$ versus log [N II]/H$\alpha$, where we mark the extreme starburst line by Ke01 with black, the composite line by Ka03 with grey, and the LINER–Seyfert separation by CF10 with yellow. The middle and right-hand panels show log [O III]/H$\beta$ versus log [S II]/H$\alpha$ and log [O I]/H$\alpha$, respectively. We mark the separation between LINER and Seyfert line (Ke06) by a pink line. In all diagrams, the narrow component is consistent with LINER and the broad component is consistent with Seyfert-like emission.

galaxy. Beyond the two galaxies, one can see [O III] emission with velocities that range between −900 and +600 km s$^{-1}$. The channel maps reveal a systematic trend kinematically, where the flux of [O III] increases towards $v \sim 0$ km s$^{-1}$ in the regions outside the primary galaxy.

We study the log [O III]/H$\beta$ratio throughout the field. For each spaxel where both H$\beta$ and [O III] are detected, we fit a single Gaussian to each emission line and measure its flux. We show this ratio in Fig. 6 using a continuous colour coding, indicated by the colour bar. The orange contours represent the stellar continuum emission, where the largest contour is the region beyond which the continuum emission is consistent with zero. The red contours represent the [O III] emission-line flux, with the largest contour marking the region beyond which [O III] is no longer detected. We note that in the central spaxels around the primary galaxy the [O III] line shows both broad and narrow components, but individual spaxels lack the necessary S/N to show both components in the H$\beta$ line. Since we fit single Gaussians to the lines, the spaxels in central regions show [O III]/H$\beta$ which is a combination of the two components found in the global spectrum (Fig. 4). Beyond about 2 kpc, we only find narrow components in both [O III] and H$\beta$. This is due to the seeing during the KCWI observation and the lack of sufficient S/N in individual spaxels. Broad components are seen in both [O III] and H$\beta$ to much larger distances, once the spaxels are summed. One can see in Fig. 6 that the extended gas (outside the primary galaxy) shows log [O III]/H$\beta \geq 0.8$, which is consistent with a Seyfert-like ionization source.

To study the extended gas properties as a function of distance from the centre of the primary galaxy, and in order to increase the S/N, we sum spaxels with the same physical distance from the central galaxy. We define a cone, in which we find most of the extended gas emission, and mark its limits with dashed white lines in Fig. 7. The opening angle of the cone is 70°. We consider only spaxels that are between these two limits. We divide the region within the cone into seven shells, indicated by different white lines in Fig. 7. In Fig. A2 in Appendix A, we show the spaxels that were used to obtain the local spectra in the different shells. We sum the spaxels within a given shell and obtain spectra as a function of distance from the centre, where we take the median distance within each shell as the distance of the shell from the centre. To appreciate the overall quality of the location-specific spectra, we show in Fig. 8 the entire KCWI spectrum of the region between 5 and 7 kpc along the gas cone.

In Fig. 9, we show the [O III] and H$\beta$ profiles of the seven shells (distances of 3.2 kpc and higher). We also show the summed spectrum of the primary galaxy (marked in the diagram as distance 0 kpc). Here we sum 3 × 6 spaxels around the galaxy, corresponding to 2 arcsec×4.1 arcsec. Thus, in total, we study the spectra of eight different regions. The narrow cores of both [O III] and H$\beta$ are shifted by 100–200 km s$^{-1}$ with respect to the systemic velocity, defined by the stars of the primary galaxy, which suggests gas that is moving towards the observer with some inclination. The summed spectra show both red and blue wings in their profiles for distances of 0–7.3 kpc, and an [O III] asymmetry detected up to 11.5 kpc. As noted previously, we find large projected velocities in the [O III] line, from approximately −1000 to +700 km s$^{-1}$ in the central regions of the galaxy. The [O III] and H$\beta$ show asymmetric line profiles which cannot be modelled with a single Gaussian. The S/N in all seven shells is high enough to integrate over the profiles to obtain the line flux. We also detect H$\gamma$ and He II λ 4686Å emission within the cone, with lower S/N. The H$\gamma$ line profile can be described by a single Gaussian, therefore we fit both H$\beta$ and H$\gamma$ with single Gaussians, tying their widths and central wavelengths to have the same systematic radial velocity and velocity dispersion. The H$\beta$ is included in this fit to gain better constraints in modelling the H$\gamma$ line, and we find similar H$\beta$ fluxes when simply integrating over the flux and when using a single Gaussian fit. We show the best-fitting Gaussian profiles in Fig. A3 in Appendix A. The He II line is even weaker than the H$\gamma$. In order to increase the S/N, we sum every pair of spectra, resulting in four (instead of eight) bins. We then fit simultaneously He II and H$\beta$, each modelled with a single Gaussian, where we tie their central wavelengths and widths. The best-fitting profiles are shown in Fig. A4 in Appendix A.

Using the best-fitting profiles for the emission lines, we measure their flux as a function of distance from the central galaxy. The upper left panel of Fig. 10 shows O III/H$\beta$ throughout the gas cone. The upper right panel shows the H$\beta$/He II ratio. The ratio increases as a function of distance for all parts of the cone beyond 6 kpc. We can also estimate the dust reddening as a function of distance from the central galaxy using the H$\beta$ and H$\gamma$ emission lines. Assuming case-B recombination, gas temperature of $10^4$ K, a dusty screen, and the Cardelli et al. (1989) extinction law, the colour excess is



Downloaded from https://academic.oup.com/mnras/article-abstract/480/3/3993/5066189 by California Institute of Technology user on 28 November 2018

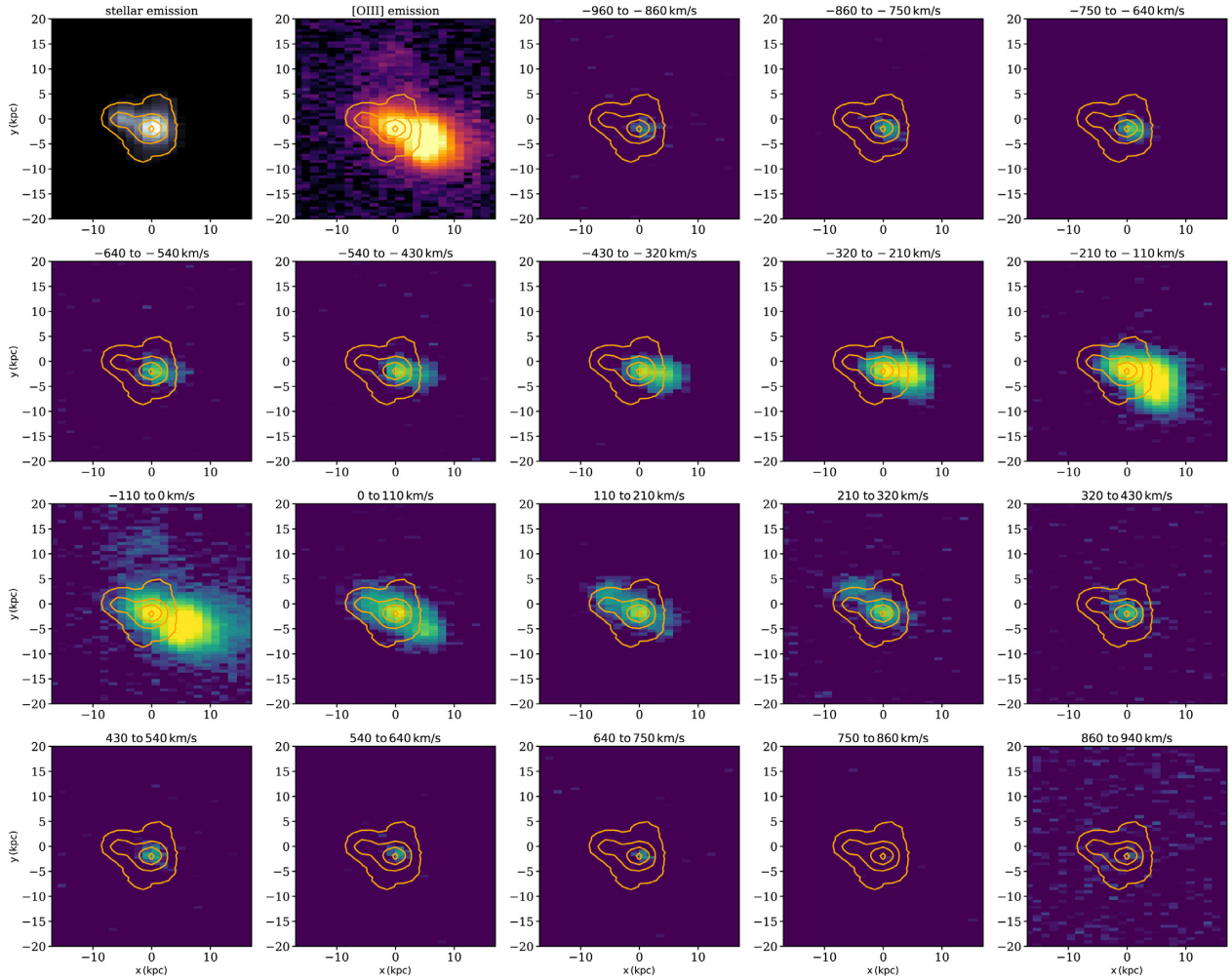


**Figure 5.** First panel: stellar continuum emission with logarithmic colour coding in the range $10^{-18}$–$10^{-17}$ erg s$^{-1}$cm$^{-2}$ pixel$^{-1}$. Second panel: integrated [O III] flux with logarithmic colour coding in the range $3 \times 10^{-19}$–$10^{-17}$ erg s$^{-1}$cm$^{-2}$ pixel$^{-1}$, where the orange contours represent the stellar continuum level and the largest contour represents the regions in which the continuum level is consistent with pure noise. Next panels: [O III] channel maps. Each panel represents a different velocity channel, compared to the systematic velocity of the stars in the primary galaxy, where we sum the [O III] flux in bins of about 100 km s$^{-1}$ per channel. The colour coding is logarithmic and is kept to a single dynamical range for all the different channels, where yellow is high flux and purple is low flux. The contours trace both the primary galaxy (located at (0, 0) kpc and [O III] systemic velocity of zero) and the secondary galaxy (located at (−5, 0) kpc and [O III] systemic velocity of 100 km s$^{-1}$). The [O III] emission extends to a distance of 17 kpc from the central galaxy, far beyond the stars in the galaxy (∼3 kpc).

given by:

$$E(B-V) = 4.53 \log\left[\frac{(\mathrm{H}\beta/\mathrm{H}\gamma)_{\mathrm{obs}}}{2.132}\right] \quad (2)$$

where $(\mathrm{H}\beta/\mathrm{H}\gamma)_{\mathrm{obs}}$ is the observed line ratio. We show $E(B-V)$ as a function of distance from the centre in the lower left panel of Fig. 10. We note that this estimate is highly uncertain due to the weak H$\gamma$ emission, and is only valid for a dusty screen geometry. We elaborate on this point in Section 4, where we present a full photoionization model for this system. In the lower right panel of Fig. 10, we show the [O III] flux along the gas cone (black).

We also examine the gas kinematics inside and outside the primary galaxy. First, we estimate the escape velocity from the galaxy using the light profile of the galaxy from the SDSS images. The exact process is described in Baron et al. (2017), and we summarize it briefly here. We assume that the mass profile is similar to the light profile, which is justified by the fact that the spectrum is dominated by a single-age population of stars. We then assume that the gas mass is at most half of the stellar mass. This is an upper limit since the gas mass observed in E+A galaxies is much lower (e.g. Rowlands et al. 2015). It is also supported by the evidence provided in the next sections. We then measure the line-of-sight FWHM of the escape velocity (see Agnello, Evans & Romanowsky 2014), which is 450 km s$^{-1}$ for our system.

In Fig. 9, we show that the [O III] and H$\beta$ emission lines exhibit both narrow and broad components. The FWHM of the broad component exceeds the escape velocity from the galaxy in all the shells, thus we suggest that the ionized gas traces a large-scale galactic outflow, driven by the central BH. To study the radial dependence of the outflow in more detail, we use the highest S/N line of [O III]. Since the line is strong enough, we divide the spaxels within the cone into 13, rather than 8, shells. For each shell, we measure $W_{80}$, which is defined as the width of the [O III] that contains 80 percent of its integrated flux: $W_{80} = v_{90} - v_{10}$, where $v_{10}$ and $v_{90}$ are the

Downloaded from https://academic.oup.com/mnras/article-abstract/480/3/3993/5066189 by California Institute of Technology user on 28 November 2018

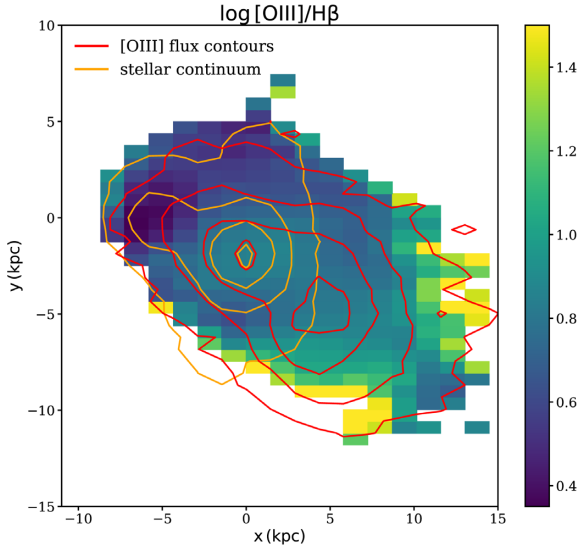


**Figure 6.** log [O III]/H$\beta$ line ratio throughout the field. Orange contours represent the stellar continuum, where the largest contour represents the regions in which the continuum is not detected. The contours trace both the primary galaxy, at (0, 0) kpc, and the secondary galaxy, at (−5, 0) kpc. The red contours represent the [O III] flux throughout the field. The secondary galaxy shows log [O III]/H$\beta \sim 0.4$, consistent with either a LINER or star-forming system. The gas in the primary galaxy and outside it shows log [O III]/H$\beta \geq 0.8$, associated with Seyfert-type emission.

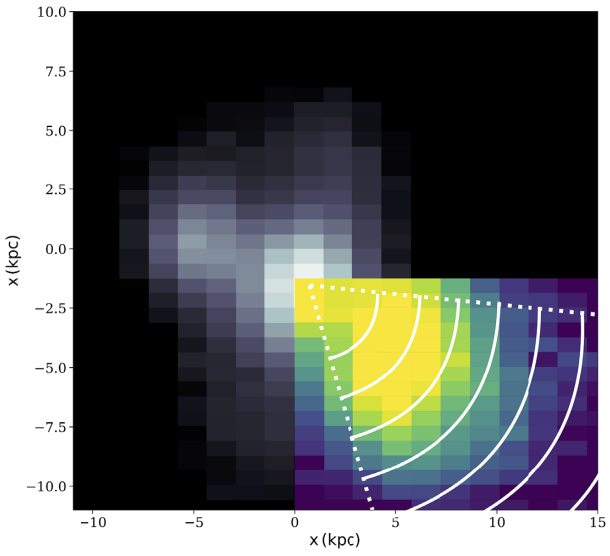


**Figure 7.** Representation of the spatial bins used to study the gas cone outside the primary galaxy. The background colour corresponds to the stellar continuum emission (in logarithmic scale) and traces the primary and secondary galaxies. The bottom right insert shows the [O III] emission outside the galaxy with logarithmic colour coding. The dashed lines mark the boundaries of the 'gas cone' discussed in the text and the solid white lines the spherical shells used to obtain integrated line emission (the actual boundaries are slightly different and determined by the individual spaxels shown in Fig. A2).

velocities that correspond to the 10th and 90th percentiles of the integrated [O III] flux. We choose to work with this definition in order to be consistent with previous studies of AGN-driven winds (e.g. Harrison et al. 2014) and to make sure that our measurements trace the broad rather than the narrow lines. For a continuous wind with spherical symmetry and a power-law radial dependence $v(r) \propto r^{-\alpha}$, $W_{80}$ will show the same radial dependence $W_{80} \propto r^{-\alpha}$, since the inclination of the system with respect to the observer will only change the normalization of the measured velocity. This is true assuming that the emissivity depends only on the distance, and that the observer does not look directly into the cone, which we confirmed numerically for our case. Therefore, $W_{80}(r)$ traces the radial dependence of the wind in the system. In Fig. 11, we show the measured $W_{80}$ for different shells (black). We find high gas velocities inside the galaxy (indicated by the grey area in the figure), and a strong drop in velocity as the gas goes out of the galaxy (at about 3–4 kpc). In most of the regions outside the primary galaxy, $W_{80}(r) \propto r^{-1/2}$, as indicated by the pink line.

While this system seems to be an ongoing major merger, hydrodynamical simulations of major mergers show that the gravitational potential during the merger due to baryonic and dark matter is similar to that of an isolated galaxy at distances larger than about 10 kpc from the centre (e.g. Sijacki, Springel & Haehnelt 2011). This suggests a roughly constant escape velocity at such distances. If the system in question has a similar behaviour, the $v(r) \propto r^{-1/2}$ we observe indicates slowing down relative to the escape velocity.

We found that the narrow cores of the emission lines in Fig. 9 have velocities of 100–200 km s$^{-1}$ with respect to the systemic velocity, defined by the stars in the primary galaxy. This suggests that the emission-line gas is moving towards us. We also found a broader kinematic component, which even without projection corrections exceeds the escape velocity from the galaxy. In Fig. 11, we found that the velocity width, W80, decreases as a function of distance from the primary galaxy. We suggest that this gas is outflowing in a direction perpendicular to the line of sight, therefore we expect small projected velocities for the wind, as we observe here. Contrary to the projected velocity, the gas location and extent will suffer from small projection corrections, thus in this scenario we observe the full extent of the outflow.

Since the complex geometry suggested here cannot be fully described by W80 and the inclination of the cone, we construct a full dynamical model where we require that the model fits the emission-line profile, in all different shells, rather than using a single threshold velocity to define the wind, as done in most other studies of this type. This model is described in Section 4.6.

## 4 MODELLING

### 4.1 BH properties

We show in Section 3.3.1 that the narrow lines within the primary galaxy are consistent with a LINER. Due to the strong resemblance of this system to the first system studied by us in Baron et al. (2017), in terms of gas properties, we argue that these emission lines are due to AGN photoionization rather than shock excitation or post-AGB stars (see Sections 4.1 and 4.2 there). The dust-corrected luminosities of [O III] and [O I] were used to measure the bolometric luminosity of the AGN using the Netzer (2009) expression:

$$\log L_{\rm bol} = 3.8 + 0.25 \log L([\rm O\,III]) + 0.75 \log L([\rm O\,I]) \quad (3)$$

This gives a bolometric luminosity of $L_{\rm bol} = 10^{44.5}$ erg s$^{-1}$ for this source. We note that the Netzer (2009) relation is based on obser-

Downloaded from https://academic.oup.com/mnras/article-abstract/480/3/3993/5066189 by California Institute of Technology user on 28 November 2018

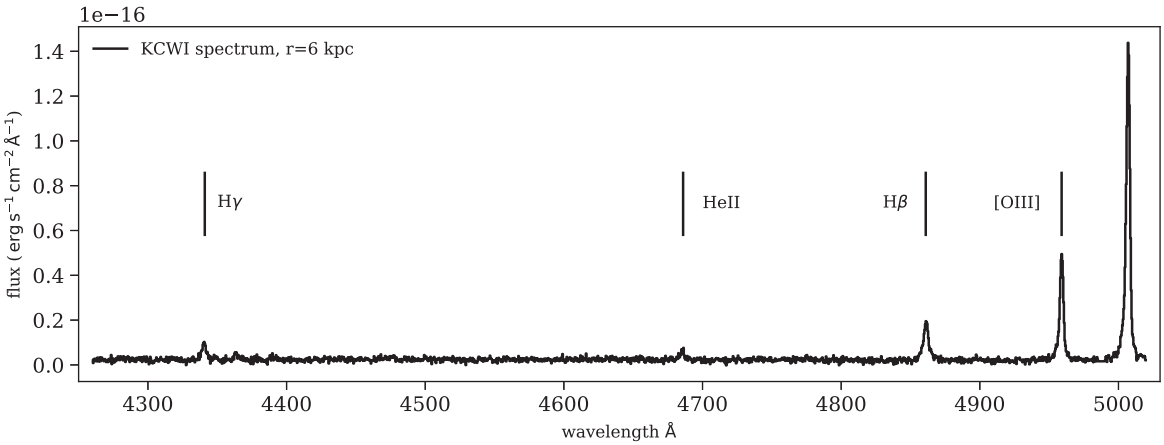


**Figure 8.** An example of a combined KCWI spectrum of the region between 5 and 7 kpc along the gas cone. The spectrum is approximately associated with the red-coloured spaxels in Fig. A2 in Appendix A. The combined spectra of other shells are of similar quality.

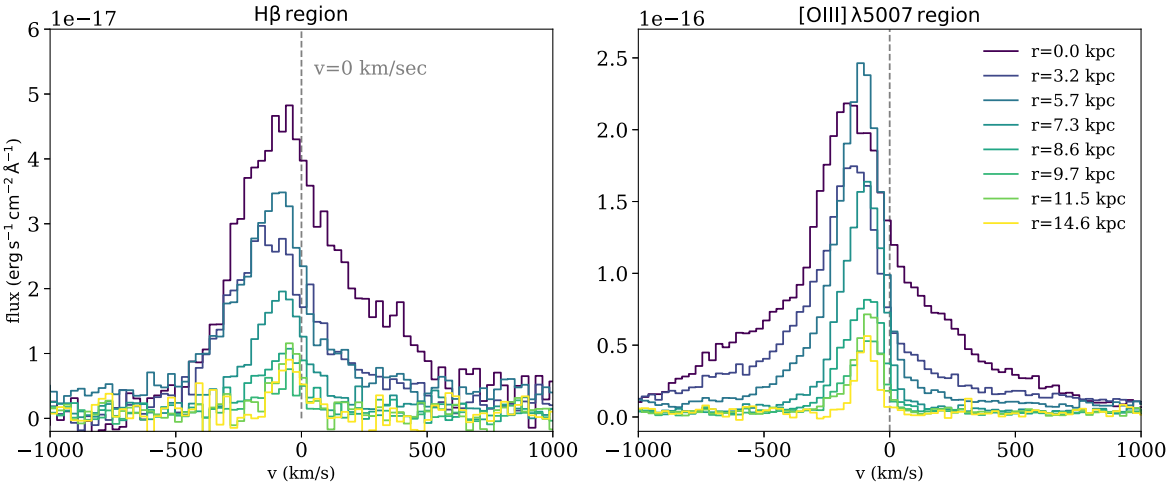


**Figure 9.** H$\beta$ (left-hand panel) and [O III] (right-hand panel) flux density as a function of distance from the primary galaxy. These spectra were obtained by summing pixels within a certain distance from the primary galaxy. The spectrum of the primary galaxy is marked as distance of 0 kpc, and is obtained by summing 3 × 6 spaxels around the centre. The *x*-axis shows the velocity, compared to systematic velocity of the stars in the primary galaxy. For distances of 0–7.3 kpc, blue and red wings are detected in the [O III] emission profile. The blue wing is detected in [O III] up to a distance of 11.5 kpc.

vations of many thousands of sources, on previous estimates of the luminosity (e.g. Heckman et al. 2004), and on detailed photoionization calculations. This relation describes the average source in the sample, and the scatter is at least 0.3 dex. We will return to this point in Section 4, where we construct a full photoionization model for the system.

The Sérsic index of the galaxy is 4.1 in the *r* band and 4.9 in *g* band, therefore the galaxy is bulge-dominated, and we can estimate the BH mass using the stellar velocity dispersion. We use the $M - \sigma$ relation from Kormendy & Ho (2013) and find a BH mass of $\log \mathrm{M/M_\odot} = 8.14 \pm 0.3$, where we assume a nominal uncertainty of a factor 2 since we measure the velocity dispersion of the entire galaxy. For solar metallicity, $L_{\mathrm{Edd}} = 1.5 \times 10^{38} (\mathrm{M_{BH}/M_\odot})\,\mathrm{erg\,s^{-1}}$ thus, from the LINER component, $L/L_{\mathrm{Edd}} = 0.01$. This ratio is an order of magnitude smaller than what we found for the first E+A galaxy, and is more consistent with type II LINERs than type II Seyferts and type I QSOs (Netzer 2009). The corresponding accretion rate, assuming mass-to-radiation conversion efficiency $\eta_{\mathrm{acc}} = 0.1$, is $\dot{m}_{\mathrm{acc}} = 0.05\,\mathrm{M_\odot yr^{-1}}$.

### 4.2 Photoionization modelling – general assumptions

In Section 3, we have shown that the primary galaxy is a post-starburst E+A galaxy that harbours an active BH. The AGN presence is reflected through the emission-line ratio [O III]/H$\beta$ and the presence of a strong He II emission, which suggests a hard ionizing continuum. We also found three ionized gas components: (1) the NLR, (2) a central unresolved broad kinematic component, with FWHM∼1000 km s$^{-1}$, and (3) gas that is located outside the primary galaxy and extends to a distance of 17 kpc, with a conic-like structure. We will refer to this component as the 'gas cone'.

The presence of a luminous AGN, the line-diagnostic diagrams and the lack of ongoing SF, all suggest that the observed emission lines are due to photoionization of the gas by the central source. In this section, we investigate the possible range of ionized gas and dust properties and present our best self-consistent photoionization models for the three components. This allows us to deduce the gas density, filling factor, covering factor, and metallicity. These properties are used later to compare our system with other type II AGN and other E+A galaxies containing active BHs. It will also

Downloaded from https://academic.oup.com/mnras/article-abstract/480/3/3993/5066189 by California Institute of Technology user on 28 November 2018

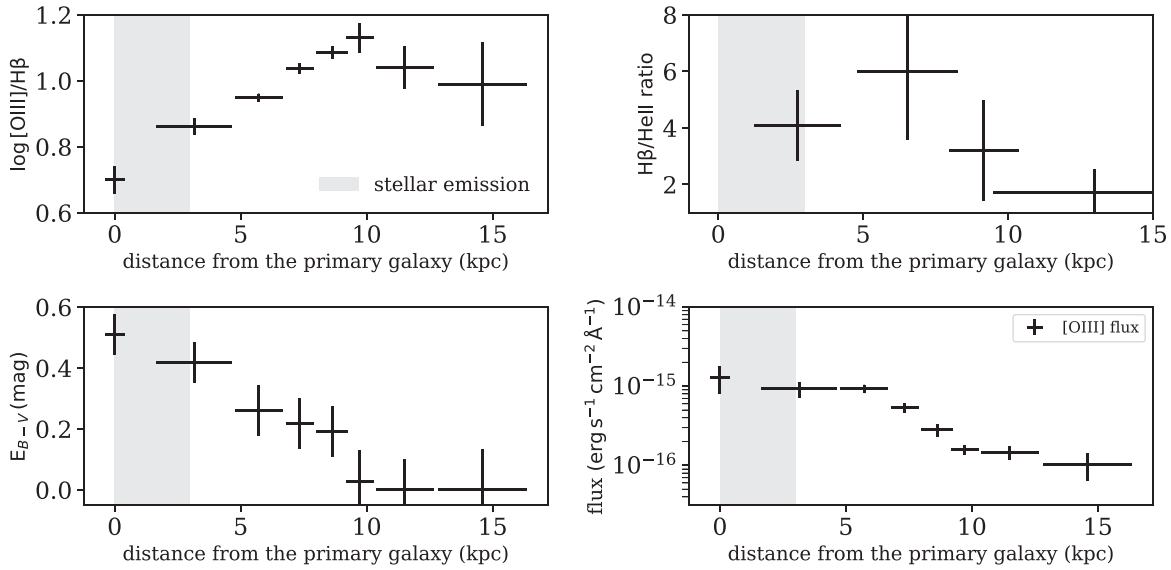


**Figure 10.** Emission-line properties as a function of distance from the central galaxy. The upper left panel shows the [O III]/H$\beta$ ratio from the primary galaxy and through the gas cone. The upper right panels shows the H$\beta$/He II ratio throughout the gas cone, where we use fewer bins to increase the S/N of the He II line. The lower left panel shows the $E(B-V)$ extracted from the H$\beta$/H$\gamma$ ratio under the assumption of a dusty screen, and the lower right panel shows measured [O III] flux in the primary galaxy and throughout the gas cone.

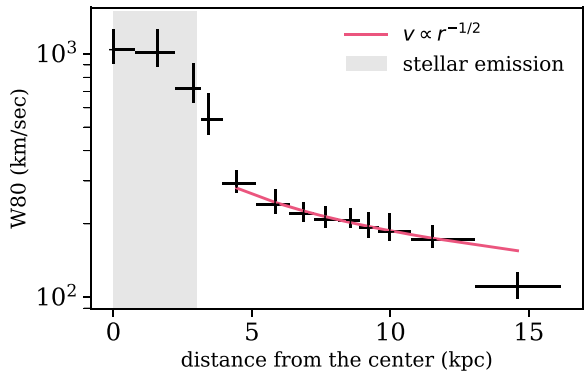


**Figure 11.** $W_{80}$[O III] as a function of distance from the centre of the primary galaxy (black). Since the [O III] line is strong enough, we divide the region into 13 shells. The uncertainties on the $x$-axis represent the sizes of the different shells, and the uncertainties on the $y$-axis represent the 85th and 75 percentiles of the flux. The gas at the outskirts of the galaxy follows a relation $v \propto r^{-1/2}$, which we mark with pink. We mark with grey the region where we detect stellar continuum emission from the primary galaxy.

provide the necessary information to deduce the mass and mass outflow rate in all observed components.

All models presented below are designed to fit the following set of conditions:

(i) The calculated H$\beta$, H$\gamma$, [O III], and He II line luminosities must agree with those observed in all the components at their various locations. They must also be consistent with the properties of the central source of ionization.

(ii) The observed line ratios must be consistent with the location-dependent ionization parameter and the dust distribution in the source.

(iii) The derived mass and mass outflow rates must be consistent with the gas density and filling factor derived in (i) and (ii) above.

(iv) The derived dust extinction must be consistent with all the above as well as with the assumed metallicity of the gas.

The photoionization models presented below depend on various assumptions which contribute to the uncertainty of the derived gas properties, and the mass and mass outflow rate estimates. The main uncertainties in our models are:

(i) The exact continuum spectral energy distribution (SED).

(ii) The metallicity and distribution of dust within the gas.

(iii) The outflowing gas distribution. As detailed below, our most successful model assumes a conic-shaped continuous wind. However, we cannot distinguish this geometry from conic-shaped motion of a large number of small optically thin clouds with a small filling factor.

Given this, the optimization problem is not convex, and we cannot define these uncertainties and propagate them properly to derive well-defined uncertainties. Nevertheless, the modelling choices we make introduce an uncertainty of at least 20 per cent to all the derived properties we list below.

### 4.3 Photoionization modelling – the gas cone

The gas cone provides most stringent constraints on the properties of the central source. Here and in what follows, we use the standard definition of the ionization parameter,

$$\mathrm{U(r)} = \frac{\mathrm{Q(Lyman)}}{4\pi r^2 n_{\mathrm{H}} c}, \quad (4)$$

where Q(Lyman) is the number of hydrogen ionizing photons per unit time, $n_{\mathrm{H}}$ is the hydrogen number density, and $c$ the speed of light. We experimented with various ionizing SEDs, all based on a combination of thin AD SED and a power-law X-ray continuum. The strong He II line observed in the source suggests a 'hard' ionizing source with a large fraction of ionizing photons above 4 Rydberg. The model chosen is consistent with a thin disc around $10^8\,M_\odot$ BH with $L/L_{\mathrm{edd}} = 0.3$. The mean energy of an ionizing photon is 38 eV. The energy slope of the X-ray source is $-0.75$ and $\alpha_{\mathrm{OX}} = 1.38$, typical of the luminosity of the central sources.



Downloaded from https://academic.oup.com/mnras/article-abstract/480/3/3993/5066189 by California Institute of Technology user on 28 November 2018

The first comparison of the photoionization calculations for the gas in the cone with observed line luminosities assumes 90 deg inclination to the line of sight. Later, in Section 4.6, we examine this assumption by comparing predicted and observed line profiles for a range of inclinations. The best-fitting inclination is very close to the one assumed here and the deviations from the numbers presented in this section are small.

The line ratios presented in Fig. 10 constrain U(r) along the cone. The [O III/H$\beta$] ratio is sensitive to the ionization state of the gas, its temperature and metallicity. The ratio ranges from 5 to 16, which sets tight constrains on the possible ionization parameters of the model to a range of $\log U = -2$ to $-0.5$. Given the estimated bolometric luminosity of the source (Section 3.3), the constraint sets the relation between the hydrogen number density, $n_H$, and the distance from the central source.

The H$\beta$/He II ratio (upper right panel in Fig. 10) gives an important clue to the ionization structure within the gas cone. The two recombination lines depend in the same way on the gas density and temperature, and their ratio does not depend on metallicity. We find that from $r \sim 6$ kpc the H$\beta$/He II ratio decreases, thus the $He^{++}$ fraction is expected to increase outwards. This can only be achieved if the ionization parameter increases outwards, which in turn requires that the hydrogen density decreases faster than $r^{-2}$. The weak He II line makes this conclusion somewhat uncertain and the only significant difference we can measure for H$\beta$/He II is between the distances of ∼6 kpc (the largest ratio) and ∼13 kpc (the smallest H$\beta$/He II). Because of this, we also considered a density law that decreases like $r^{-2}$ and results with a roughly constant Hb/He II. As discussed below, the very fast decrease of density with distance is supported by the more robust, easier to measure [O III]/H$\beta$ line ratio.

The luminosities of the observed emission lines [O III], He II, and H$\beta$ as a function of distance from the central source (see e.g. bottom right panel in Fig. 10) set additional constraints on the model. While for a constant temperature, the line luminosities increase quadratically with the density, too large density and filling factor increase the gas opacity and result in a radiation bound configuration, where at large distances, the gas becomes neutral and does not emit line radiation. Thus, the highly ionized strong emission-line gas at large distances suggest a density bound system, where only part of the ionizing radiation is absorbed by the gas (i.e. the cone must be optically thin).

Following these considerations, we model the gas cone as a single gas cloud that starts at a distance of 1 kpc from the central source and extends to 15 kpc, with density and filling factor that are modelled as simple power laws with the distance. It is unclear where exactly is the transition between gas that resides inside the galaxy and gas that is outside. Since the stellar continuum is no longer detected at about 3 kpc, we will compare the model to observations from 3 to 15 kpc. We take the covering factor to be 0.1, since the gas cone shows an opening angle of about 70° (projected on the sky).

As explained in Section 4.1, the bolometric luminosity of the AGN, based on the [O III], [O I], and H$\beta$ lines in the NLR, is estimated to be $L_{bol} = 10^{44.4}$ ergs$^{-1}$. These relations represent the mean of a very large number of type II AGN and the uncertainty on this number, as judged from the scatter in the relationship, is at least 0.3 dex (see Netzer 2009). Therefore, we consider a range of luminosities between $L_{bol} = 10^{44}$ and $10^{45}$ ergs$^{-1}$ with the SED described earlier.

Next, we consider the gas density and filling factor. For the initial density at 1 kpc, we explored the range $n_H = 10$–$500\,cm^{-3}$, and for the radial dependence $n_H \propto r^{-2}$ to $n_H \propto r^{-3.5}$ (a steeper density law will not give sufficient flux at large distances). We consider a filling factor at the illuminated face of the cloud in the range $f = 0.003$ to 0.1, and a radial dependence in the range $f \propto$const to $f \propto r^2$. These choices are motivated by the constraints of line intensity and line extent and the various parameters were allowed to change until finding the best agreement with the observations. We note that for a specific choice of $n_H$ and its radial dependence, there is little freedom in the choice of $f$ and its radial dependence. The two parameters are highly correlated due to the fact that the line luminosity depends on the product $f n_H^2$. Therefore, the range in radial dependence of the filling factor is set by the density power law. One can expect a rising power law in the filling factor in a case where gas in the galaxy is swept by the propagating wind.

Finally, we experimented with different amounts of dust absorption and extinction by changing the gas metallicity from 0.3 to 3 times solar. Lacking additional constraints, we assume ISM-type grains with the relevant depletion from the gas phase.

We run a grid of models with version 17.00 of CLOUDY (Ferland et al. 2017). The parameters of the models vary within the ranges specified above, and the comparison with the observations was done in seven shells that were defined by the observation described in Section 3.3.2 (Fig. 7). The comparison includes: [O III], He II, H$\beta$, and H$\gamma$.

In Section 3.3.2, we estimated the dust reddening along the gas cone using the H$\beta$/H$\gamma$ ratio, assuming a dusty screen. However, the dust used in the photoionization model is mixed with the gas. This will result in different attenuation of the emitted radiation partly because the emitting gas is spread throughout the entire volume and partly because such dust will only absorb radiation and will not scatter it out of the line of sight. Therefore, the two geometries give different H$\beta$/H$\gamma$ ratios for a given amount of dust. To untangle this complex situation, we first extract the *emergent* line luminosities of the model. These luminosities are the result of dust absorption within the gas cone. We use the *emergent* H$\beta$/H$\gamma$ line ratio and compare it to the observed one. We then added a dusty screen between the gas cone and the observer if the *emergent* line ratio require such a component. The additional screen added in this way must be associated with neutral gas that is not exposed to the central source of radiation. We compute the value of $E(B-V)$ by matching the model results with the observations. We then compare these luminosities to the observed luminosities in different shells.

Given all that, the parameters of the best-fitting model are a central source with a bolometric luminosity of $L_{bol} = 10^{45}$ ergs$^{-1}$, and SED typical of a high accretion rate thin disc, as explained earlier. The density in the model is $n_H = 160\,(\frac{r}{1kpc})^{-3}\,cm^{-3}$, the filling factor is $f = 0.005\,(\frac{r}{1kpc})^{1.4}$, and the metallicity is half-solar with interstellar medium (ISM)-type grains. We show in Fig. 12, the observed [O III]/H$\beta$ ratio compared to the predicted ratio (upper left panel), and a comparison between the observed line luminosities to the luminosities predicted by the model. In all three lines, we show both the *emergent* luminosity (i.e. after accounting for internal reddening within the cloud; blue) and the *emergent* luminosity after additional extinction by a dusty screen. Clearly, our model reproduces all the observations quite well. The exception is H$\beta$ line luminosity, which is systematically too low in the model.

The model presented in Fig. 12 is the only model, within the explored range of parameters, that reproduces the measured [O III] and the H$\beta$ luminosities. All other models fail to do so with differences between model and observations as large as a factor of 5–30. Some of these failing models succeed in predicting the [O III] luminosity and failed for the H$\beta$ and He II luminosities (by more than an or-

Downloaded from https://academic.oup.com/mnras/article-abstract/480/3/3993/5066189 by California Institute of Technology user on 28 November 2018

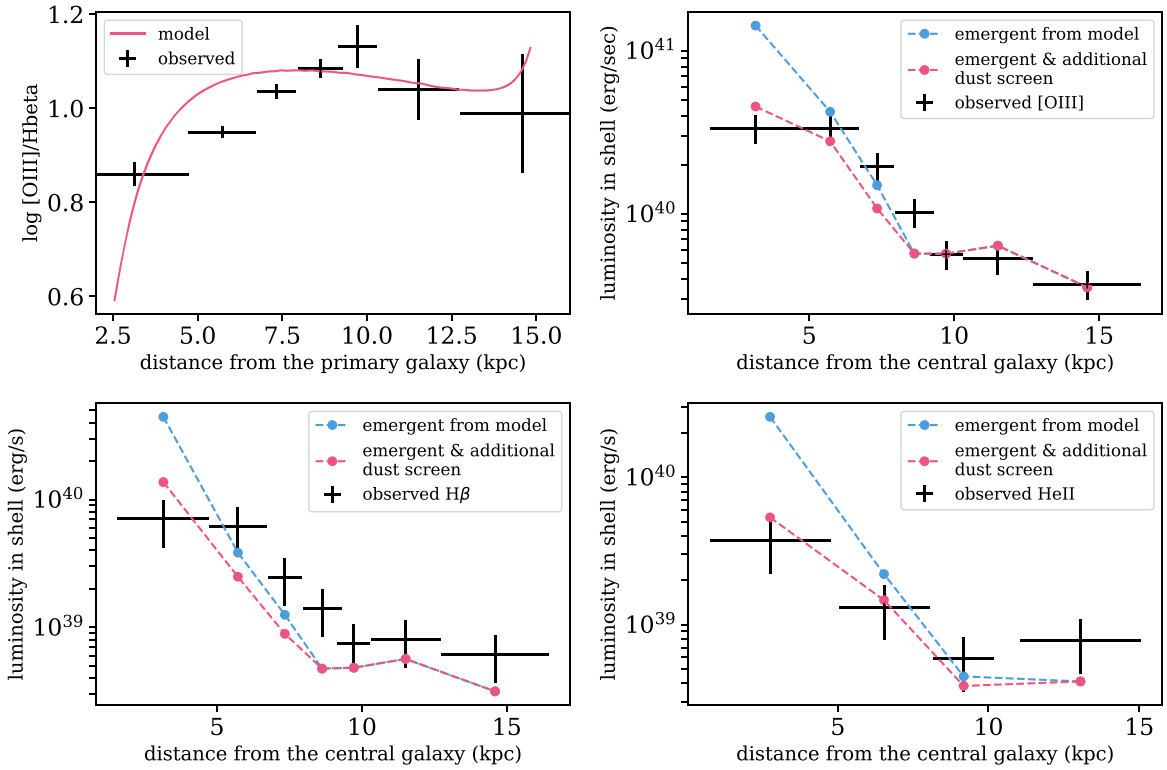


**Figure 12.** Comparison of various observed properties of the gas cone to the best photoionization model. The model is composed of a central source with a bolometric luminosity of $L_{bol} = 10^{45}$ erg sec$^{-1}$, and with the SED described in the text. The gas has a spherical symmetry and extends from 1 to 15 kpc, with a covering factor of 0.1. The density is $n_H = 160\,(\frac{r}{1kpc})^{-3}$ cm$^{-3}$ and the filling factor $f = 0.005\,(\frac{r}{1kpc})^{1.4}$. The metallicity is half solar with ISM-type grains. The upper left panel compares the observed log [O III]/H$\beta$ ratio (black crosses) to that of the model (red line). The rest of the panels compare the observed line luminosities (no dust correction; black crosses) to the *emergent* line luminosities before (blue) and after (red) applying additional reddening due to a dusty screen with E($B-V$) obtained from the observed H$\beta$/H$\gamma$ ratios.

der of magnitude). Others result in an almost neutral cloud, with very low [O III] and He II luminosities and with acceptable H$\beta$ luminosities. We also note that the best model in which an additional dusty screen (which is not part of the gas cone) is not necessary has a bolometric luminosity of $L_{bol} = 10^{45.4}$ ergs$^{-1}$ and a density of $n_H = 275\,(\frac{r}{1kpc})^{-3}$ cm$^{-3}$. This model gives H$\beta$ line luminosity which is consistent with observations, but fails to reproduce the line luminosities observed in the NLR, which is described in the following section.

### 4.4 Photoionization modelling – the NLR

Next we model the NLR gas using the luminosity and SED obtained from the best-fitting model of the gas cone. The narrow lines are consistent with a LINER, and the emission-line ratios we observe (see Fig. 4) require an ionization parameter of log U $\approx -3.6$ for the chosen SED. We choose a thin gas slab, with a density of $n_H = 10^4$ cm$^{-3}$ at a distance of 1 kpc, which reproduces the observed emission-line ratios to within 0.2 dex. Since the NLR is not fully resolved by the observations, this combination of $n_H$ and $r$ is not unique. The covering factor that is necessary to match the observed and the predicted line luminosities is 0.042. For the (rather arbitrary) chosen column density of $10^{21.5}$ cm$^{-2}$, the amount of reddening matches the observations and there is no need for an additional dust screen.

All the properties noted above are consistent with observations of NLR in type II AGN (see Netzer 2009, Heckman & Best 2014), with other E+A galaxies showing AGN-driven winds (Baron et al. 2017), and with luminous LINERs observed in the local universe (Pović et al. 2016).

### 4.5 Photoionization modelling – the high velocity central component

Finally, we model the broad kinematic component in the central part of the galaxy, using the luminosity and SED of the best-fitting model of the gas cone. The broad lines are consistent with a Seyfert-type spectrum (see Fig. 4), with an ionization parameter of about log U $= -2.4$. We model the broad kinematic component as a thin shell at a distance of 0.85 kpc (see below), with a density of $n_H = 10^3$ cm$^{-3}$. This choice reproduces the emission-line ratios to within 0.2 dex, and for a covering factor of 0.3 it also reproduces the observed emission-line luminosities. A covering factor of 0.3 is rather large for an NLR-type gas (see Netzer 2009), but is consistent with an outflow with a large opening angle. It is also consistent with the covering factor found for the outflowing component in Baron et al. (2017), which is 0.5.

As explained in Section 3.3.2, the broad kinematic component is either unresolved or marginally resolved, with a diameter that is not larger than ∼1 kpc. While we do not have a strong constraint on the location of this gas, the required ionization parameter sets a tight constraint of $\sim 6.2 \times 10^{45}$ cm$^{-1}$ on the product $n_H r^2$. There is a range of possible distances and gas densities that satisfy this constraint, and each of these will produce a model that is consistent with the observations. The range, 0.1–1 kpc, represents a real uncertainty on



Downloaded from https://academic.oup.com/mnras/article-abstract/480/3/3993/5066189 by California Institute of Technology user on 28 November 2018

the mass and mass outflow rate of this component. We will use these numbers when estimating these properties in Section 4.7.4 below.

### 4.6 Dynamical modelling – the gas cone

We now model the dynamics of the gas in the gas cone. Given the PSF, we focus on lines of sight with a projected distance larger than 5 kpc. In Section 3.3.2 (Fig. 11), we found that $W_{80}(r) \propto r^{-1/2}$, which means that the velocity of the wind is given by $v(r) = v_0 \cdot \left(\frac{r}{1\,\mathrm{kpc}}\right)^{-1/2}$. We assume the same geometry as in the photoionization model – a cone with an opening angle of 70°, ranging from 0 to 17 kpc. We assume that the velocity, emissivity, and density depend only on the distance from the centre and use the line emissivity and gas density from the best-fitting photoionization model presented in Section 4.3. For a given line of sight, the emission-line profile will depend on the inclination of the cone with respect to the line of sight. For a dustless gas and an inclination of 90°, the emission-line profile is a double-horn symmetric profile around $v = 0$ km s$^{-1}$, while for an inclination of 0° (looking into the cone) the entire line profile is blueshifted with respect to the systematic velocity, assuming the turbulent velocity is smaller than the radial velocity. For a dusty gas, the dust absorbs the emission lines originating in the farthest side of the cone more than in the closer side (with respect to the observer), as we discuss below.

Our goal is to fit the observed emission-line profiles as a function of projected distance from the galaxy, and extract the best-fitting $v_0$ and inclination. We use the highest S/N line, [O III]λ5007Å, and examine five bins of projected distances, from 5 to 15 kpc. Generally, there are two angles which affect the resulting image, one of which is directly observed (see Fig. 5), and it is roughly 45 deg with respect to the west–east axis. We therefore rotate the coordinate system so that the inclination with respect to this angle will be zero. We therefore have a single inclination angle to fit.

We start from five regions that are observed as five partial thick shells. Given an inclination with respect to the line of sight, we project them back onto the real cone. This results in five regions inside the cone which are not spherical shells. Since the model provides the line emissivity at each location within the cone, all points inside the projected shells can be combined to give the predicted line emission, prior to dust extinction, in all five regions. The velocity of the gas within each projected shell is projected back onto the line of sight to obtain the emission-line profile, which we compare with observations. Each projected shell contains dusty gas, thus we need to take into account the dust extinction when constructing the line profile. The dust is distributed within the cone with the same radial dependence as the gas density (which we take from the photoionization model). For large enough inclinations, the dust will absorb the redshifted part (gas which is moving away) more than the blueshifted part (gas which is moving towards the observer). We use the gas density from the photoionization model and for each region within a given projected shell, we compute the gas column density from this region to the edge of the cone. We use this column density to determine the dust reddening of each such region. We apply the dust reddening to the intrinsic emissivity of each region before adding it to the combined line profile. Finally, we convolve the resulting emission-line profile with a Gaussian with a standard deviation of $\sigma_{\mathrm{turb}}$, representing the (unknown) turbulent velocity in the gas.

The dust extinction in the dynamical model is due to *internal* dust which is mixed with the gas in the cone. This dust is not the dusty screen discussed in Section 4.3. The main difference is that the dusty screen absorbs and scatters photons out of the line of sight, and affects the blue and red parts of the emission lines originating in the cone in a similar manner. The internal dust cannot be treated with equations (1) and (2). In the photoionization model, internal dust is directly taken into account, such that the *intrinsic* line emission is absorbed by internal dust, resulting in *emergent* line emission, which is the quantity plotted here. In most of the shells, this is a large effect as evident from the observed line luminosities which indicate large column densities.

The result of this procedure is an emission-line profile, which depends on the distance and on three free parameters: (1) $v_0$ – the wind velocity at 1 kpc, (2) $i$ – the inclination of the gas cone with respect to the observer, and (3) $\sigma_{\mathrm{turb}}$ – the turbulent velocity dispersion in the gas. We show in Fig. 13 such a model, with $v_0 = 800$ km s$^{-1}$, $i = 80°$, and $\sigma_{\mathrm{turb}} = 25$ km s$^{-1}$. We mark the observed [O III] emission line with black, and the modelled emission-line profile with pink, before and after applying the dust reddening along the line of sight (dotted and solid lines, respectively). We find reasonable fits to the emission-line profiles for $v_0$ in the range 700–900 km sec$^{-1}$, $i$ in the range 75°–85°, and turbulence velocity dispersion of 20–30 km s$^{-1}$. As clearly seen in the diagram, dust attenuation of the red wing of the line in all shells is key to the good agreement between model and observations. This shows that the outflowing gas with large velocities is observed with small velocities, due to the inclination of the system and the extinction by internal dust. According to our model, without internal dust, W80 is about 400 km sec$^{-1}$ outside the galaxy, roughly twice the observed value.

As noted earlier, the best-fitting photoionization model for the gas cone presented in Section 4.3 is calculated under the assumption that the inclination of the cone with respect to the observer is 90°. However, we find that for inclinations in the range 70°–90°, the projection of the best-fitting photoionization model changes the emission-line luminosities and ratios by no more than 0.05 dex. Therefore, the best-fitting photoionization model is consistent with the best-fitting dynamic model of the wind.

### 4.7 Mass and mass outflow rates

The models presented above are detailed enough to deduce the mass and mass outflow rate in each of the four components: the gas cone, the neutral dusty screen, the NLR, and the central high velocity gas. Below we derive mass and mass outflow rate for each using the best-fitting photoionization models and the detailed velocity maps presented in Figs 5 and 11. The uncertainties on the mass and mass outflow rates are dominated by the uncertainties in our photoionization models, and are at least 20 per cent (see Section 4.2). The geometry of the emitting gas is modelled through the fit to the observed line profiles and luminosities and therefore does not add significantly to the overall uncertainty.

#### *4.7.1 The gas cone*

As explained in Section 4.3, we modelled the gas outside the galaxy as a cone with an opening angle of 70°. The mass in the gas cone is given by:

$$M_{\mathrm{gas}} = 4\pi\mu m_{\mathrm{H}} C_f \int_{3\,\mathrm{kpc}}^{15\,\mathrm{kpc}} r^2 n_{\mathrm{H}}(r) f(r) \mathrm{d}r \quad (5)$$

where $\mu$ is the mean molecular weight, $m_{\mathrm{H}}$ is the hydrogen mass, $C_f$ is the distance-independent covering factor (which is simply set



Downloaded from https://academic.oup.com/mnras/article-abstract/480/3/3993/5066189 by California Institute of Technology user on 28 November 2018

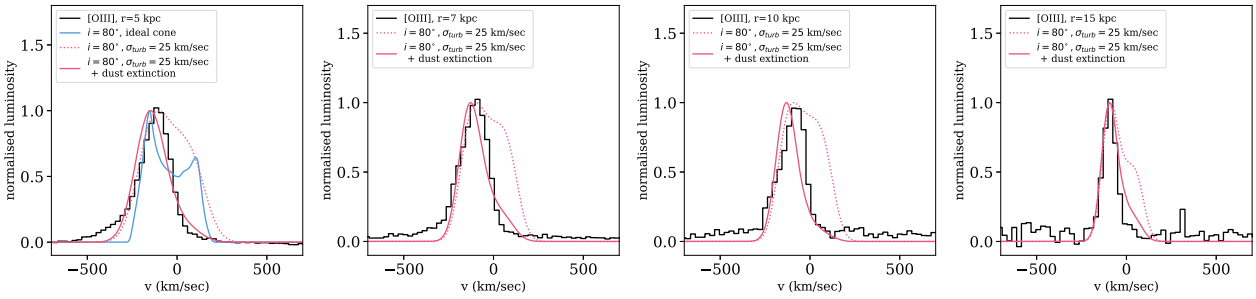


**Figure 13.** Comparison of the observed [O III] emission-line profile (black) with a dynamic model of an expanding gas cone. The gas in the cone is expanding with a velocity of $v(r) = 800 \cdot \left(\frac{r}{1\,\mathrm{kpc}}\right)^{-1/2}$ km s$^{-1}$, and its emissivity and density are calculated from the best-fitting photoionization model with various assumptions about dust extinction and turbulent motion. The inclination of the cone with respect to the LOS is $i = 80°$. The left-hand panel shows an ideal cone (without turbulence and dust extinction) with the distance-dependent emissivity, which we mark with blue. The other panels show the emission-line profile before and after applying reddening along the line of sight, which we mark with dotted and solid pink lines, respectively. The velocity dispersion due to turbulent motion is $\sigma_{\mathrm{turb}} = 25$ km s$^{-1}$ in all cases.

by the opening angle of the cone), $n_{\mathrm{H}}(r)$ is the distance-dependent hydrogen density, and $f(r)$ the distance-dependent filling factor. The integrated mass to a given distance from the central galaxy is proportional to $r^{1.4}$. We choose the integration limits to be from 3 kpc (approximately where we no longer detect stellar continuum emission) to 15 kpc. The outer boundary of the detectable wind is probably somewhere between 15 and 17 kpc. Using $r = 15$ kpc as the upper limit, and the density and filling factors obtained in Section 4.3, we get a gas mass of $M_{\mathrm{gas}} \approx 7 \times 10^8\,\mathrm{M}_\odot$. For $r = 17$ kpc, we find $M_{\mathrm{gas}} \approx 10^9\,\mathrm{M}_\odot$.

Our best-fitting photoionization model slightly underestimates the H$\beta$ emission-line luminosity (see Fig. 12). A model that does not underestimate the H$\beta$ luminosity (and hence will slightly overestimate the [O III] luminosity) requires higher gas density and larger total mass.

Assuming that the wind in the gas cone is continuous, the mass outflow rate is:

$$\dot{M} = 4\pi\mu m_{\mathrm{H}} r^2 C_f n_{\mathrm{H}}(r) f(r) v(r) = \mathrm{const} \quad (6)$$

where $v(r)$ is the wind velocity, assuming spherical symmetry, where the opening angle is not changing with the distance. Using the best-fitting power laws from the photoionization model to extract the radial dependence of the wind velocity, we find $v(r) \propto r^{-0.4}$, very close to the relation we observe using the [O III] emission-line profile, $W_{80} \propto r^{-0.5}$ (see Section 3.3.2 and Fig. 11). Under these assumptions, the profiles inferred from the photoionization model are consistent with the observations. Alternatively, we can state that the photoionization model and the observed gas kinematics imply that the wind in the gas cone is a continuous flow. This empirical result is hard to explain since it means that the gas reservoir close to the BH can last a period of well over $10^6$ yr. Below we use these numbers to put limits on the time that the BH is active (Section 5.2), and to infer the fate of this outflowing gas (Section 5.3).

Using the location-dependent gas density and filling factor from the best-fitting photoionization model, the mass outflow rate is $\dot{M} \approx 24\,\mathrm{M}_\odot\mathrm{yr}^{-1}$. We integrate from 3 to 17 kpc over the velocity of the gas and find that the kinetic power of the wind is roughly $8.5 \times 10^{-3} L_{\mathrm{bol}}$.

### 4.7.2 *The neutral dusty screen*

We found in Section 4.3 that in order to be consistent with the observations one must add a dusty screen between the gas cone and the observer. We require this screen to be neutral, as it does not contribute to the observed line emission. The additional dust reddening is needed in the first three shells, with $E(B-V) = 0.3$ mag at 3.2 kpc, $E(B-V) = 0.13$ mag at 5.7 kpc, and $E(B-V) = 0.1$ mag at 7.3 kpc. For solar metallicity, the corresponding column densities are $N_{\mathrm{H}} = E(B-V) \times 5.6 \cdot 10^{21}\,\mathrm{cm}^{-2}$. The minimal mass is obtained by adding three screens covering exactly the corresponding parts of the cone. Each screen is modelled as a rectangle that corresponds to the size of the shell. This gives $M_{\mathrm{screen}} \sim 1.4 \times 10^8\,\mathrm{M}_\odot$. As indicated, the geometry of the dusty neutral screen is unknown, as it is not traced by optical emission lines. Therefore, the assumed geometry is uncertain, and the measured maximum mass can be 2–3 times larger, depending on the other parts of the galaxy obscured by such a screen and the exact geometry. Thus, the neutral screen mass is 2–5 times smaller than the mass in the cone albeit with a large uncertainty.

### 4.7.3 *The NLR*

For the NLR, we assume a spherical thin shell geometry. The thickness of the shell is only limited by the requirement of a radiation bounded gas. For a column density of $N_{\mathrm{H,NLR}} = 10^{21.5}\,\mathrm{cm}^{-2}$, the mass is:

$$M_{\mathrm{NLR}} = 4\pi C_{f,\mathrm{NLR}} r_{\mathrm{NLR}}^2 N_{\mathrm{H,NLR}} \mu m_{\mathrm{H}} \quad (7)$$

where $C_{f,\mathrm{NLR}} = 0.042$ is the NLR covering factor, $r_{\mathrm{NLR}} = 1$ kpc, and $N_{\mathrm{H,NLR}} = 10^{21.5}\,\mathrm{cm}^{-2}$. The NLR gas mass is therefore $M_{\mathrm{NLR}} \approx 1.5 \times 10^7\,\mathrm{M}_\odot$.

### 4.7.4 *The central high velocity ionized component*

The photoionization model presented in Section 4.5 is not unique because of the uncertainty on the location of the gas. The procedure we use to estimate the mass and the mass outflow rate of the ionized gas is similar to the one used by Baron et al. (2017), which is based on the known ionization parameter and hence the known value of $n_{\mathrm{H}} r^2$ ($6 \times 10^{45}\,\mathrm{cm}^{-1}$, see Section 4.5). The ionized gas mass is directly related to the H$\alpha$ luminosity (see e.g. Soto et al. 2012 and Baron et al. 2017):

$$M_{\mathrm{out}} = \frac{\mu m_{\mathrm{H}}}{\gamma n_{\mathrm{H}}} L_{\mathrm{H}\alpha} \quad (8)$$

where $\gamma = 3.56 \times 10^{-25}\,\mathrm{erg\,cm^3\,s^{-1}}$ for case B recombination and $T_{\mathrm{e}} \sim 10^4$ K (Osterbrock & Ferland 2006), and $L_{\mathrm{H}\alpha} = 4.5 \times 10^{42}$



Downloaded from https://academic.oup.com/mnras/article-abstract/480/3/3993/5066189 by California Institute of Technology user on 28 November 2018

erg $s^{-1}$. This results in a mass estimate which depends only on the location of the gas:

$$M_{\rm out} \approx 2.5 \times 10^7 \left(\frac{\rm r_{out}}{1\,\rm kpc}\right)^2 \rm M_\odot \quad (9)$$

where $r_{\rm out}$ is in the range 100 pc to 1 kpc (see Section 4.5). The upper limit on the mass, $2.5 \times 10^7\,\rm M_\odot$, is 50 times lower than the mass in the gas cone, with a kinetic power of roughly $1.5 \times 10^{-3} L_{\rm bol}$. A possible interpretation is that the AGN has already driven most of the primary gas outside of the galaxy. Obviously, the fast moving ionized gas can be radiation bounded, in which case the total mass of this component, and its kinetic energy, must include an additional contribution from neutral gas at the back side of the outflowing material.

The mass outflow rate for this component is given by $\dot{M}_{\rm out} = M_{\rm out}/t_{\rm out}$, where $t_{\rm out} = r_{\rm out}/v_{\rm out}$. We take $v_{\rm out}$ as the velocity of the peak of the broad emission relative to the peak of the narrow, added to the width of the broad emission, $v_{\rm out} = v_{\rm peak,broad} + \sigma_{\rm broad} = 550\,\rm km\,s^{-1}$. The resulting outflow rate is:

$$\dot{M}_{\rm out} \approx 16 \left(\frac{\rm r_{out}}{1\,\rm kpc}\right) \rm M_\odot yr^{-1}. \quad (10)$$

Taking $v_{\rm out} = W_{80}/1.3$ (see Harrison et al. 2014) instead, results in $v_{\rm out} = 830\,\rm km\,s^{-1}$, which increases the outflow rate by a factor of 1.5 to $\dot{M} \approx 24\,\rm M_\odot yr^{-1}$, similar to the mass outflow rate in the gas cone. Given the limits on the winds location, we find that the mass outflow rate for this system is more than an order of magnitude lower than what we found in Baron et al. (2017) for the central broad component in the E+A galaxy SDSS J132401.63+454620.6 (the maximum in that case was $120\,\rm M_\odot yr^{-1}$). Most of the difference between the two E+A galaxies is due to the fact that the broad H$\alpha$ luminosity in the present case is about an order of magnitude smaller compared to the case presented in Baron et al. (2017). Again, these calculations provide only lower limits since they do not take into account neutral gas at the back side of the flow.

## 5 DISCUSSION

The observations and models presented in this paper link the central AGN with high velocity ionized gas flows in two regions: a central region with a distance of 1 kpc or less from the AGN, and a conical-shaped region that extends up to about 17 kpc from the centre of the primary galaxy. Our IFU measurements, and detailed dynamical and photoionization modelling of this gas, clearly indicate an AGN-driven flow. To the best of our knowledge, this is the very first time that continuous, wind-type flows, that are accurately timed (through the known stellar population), and with such well-determined mass and mass outflow rates, are reported. It is also the clearest case, so far, showing that the amount of gas removed by the wind, is most of the gas remaining in the system after the quenching of SF. This seems to be a classical example of an AGN feedback where quenching is directly related to gas removal from the system.

Given the likely history of the system in question (merger and ULIRG), we must also consider two alternative scenarios related to the origin of the ionized gas outside the galaxy. We focus on the gas in the cone where the observational and modelling constraints are tighter and where the mass of the ionized gas is the largest.

### 5.1 Alternative origins for the gas in the cone

#### *5.1.1 Gas stripped from the companion galaxy*

One possible interpretation of the existence of a significant amount of gas outside the primary galaxy concerns the interaction itself. It is possible that the observed gas was stripped from the companion galaxy during its close pass near the primary galaxy, about 100–200 Myr ago. According to this scenario, the stripped gas cooled down and expanded until the AGN turned on, and photoionized this gas. There are two possible configurations which we consider. In the first case, the gas is falling onto the primary galaxy, and in the second case, the gas is neither an outflow nor an inflow, and is moving towards the observer with the same velocity it had when it was detached from the secondary galaxy.

An inflow with a large opening angle can, in principle, produce both blueshifted and redshifted emission lines, with respect to the systematic velocity of the primary galaxy. The cone-like structure is more difficult to explain but even this assumption runs into real difficulties. For an outflowing cone, the blueshifted part is produced by the closest region in the cone, and the redshift part by the farthest region in the cone. For an ideal cone, viewed at an inclination of 90°, both of them produce a double-horn, symmetric around 0 km $s^{-1}$, emission-line profile. However, since the gas is dusty, the dust absorbs the emission lines originating on the far side more than on the near side. Therefore, for an inclination close to 90°, for an outflowing gas cone, the dust will absorb the redshifted part of the emission-line profile, while for an inflowing cone, the dust will absorb the blueshifted part of the profile. Fig. 13 clearly shows that the redshifted part is absorbed, while the blueshifted part is not. Therefore, dynamical considerations, based on the line profiles, rule out this explanation.

A cone with an inclination of close to 180°, where the line of sight points straight to the in-falling gas, will produce a primarily blueshifted emission. This scenario cannot account for the redshifted emission. Furthermore, this scenario requires large projection corrections, which result in an infall velocity which exceeds greatly the expected free fall velocity of the gas at a given distance from the primary galaxy.

In the second scenario, where the gas is neither an outflow nor an inflow, the gas moves towards the observer with roughly the same velocity as the velocity of the secondary galaxy, when it was detached during the interaction. In this scenario, the conical shape is the result of the illuminated pattern of the central source (the opening in the central torus) and dust absorption in the cone will extinct the red and the blue sides of the line in the same way. This is not consistent with the large column of ionized gas needed to explain the line luminosities. Such columns imply large column of dust which suggests that the emission we see originates, preferentially, in the closest layer of the shell. This scenario cannot explain the observed redshifted part of the emission line. Furthermore, the dynamical time-scale of the merger is of order hundreds Myr, thus the gas must have been detached from the secondary galaxy a few hundreds Myr ago, when the secondary galaxy was (presumably) on the west-south side of the primary galaxy. When detached, the gas had some initial density and turbulent velocity dispersion. For any acceptable gas density and velocity dispersion, the gas would have been dispersed in less than roughly 50 Myr (e.g. Hani et al. 2018), with its density dramatically decreasing. After roughly 50 Myr, the gas density is too low to produce the ionized emission lines we observe. The fact that we currently observe ionized emission lines in this region suggests that the gas stayed in this location less than 50 Myr, much

Downloaded from https://academic.oup.com/mnras/article-abstract/480/3/3993/5066189 by California Institute of Technology user on 28 November 2018

shorter than the time since the secondary (presumably) passed in this region.

#### *5.1.2 Starburst-driven outflow*

The observed gas outside the primary galaxy may also be due to SNe-driven winds during the recent starburst. Such a scenario was suggested by Heckman et al. (2017) to explain possible differences of the CGM properties observed in 17 E+A post-starburst galaxies, compared to a control sample of non-post-starburst systems. During the starburst, SNe-driven winds can accelerate gas to substantial velocities, which are large enough to remove the gas from the system (see Heckman et al. 2017 and Heckman & Thompson 2017 for a detailed review). Such observed starburst-driven winds are multi-phased, where each phase differs in its temperature, density, and velocity. The warm-ionized phase, which is traced by optical emission lines, shows wind velocities of hundreds to a thousand km $s^{-1}$, without correcting for projection effects. Winds that are traced by interstellar absorption lines show roughly the same velocities (see Heckman & Thompson 2017 for a full discussion of properties and caveats).

The best-fitting stellar population synthesis model for our system suggests a starburst that started 400 Myr ago, and decreased exponentially to less than 10 per cent of its initial SFR values after 200 Myr. Therefore, most of the core-collapse SNe occurred roughly 300 Myr ago. Assuming a typical outflow velocity of 500 km $s^{-1}$, the gas would have travelled 150 kpc by now, far beyond the region where we detect the outflow. Alternatively, in order to detect SNe-driven wind at a distance of 17 kpc from the centre of the primary galaxy, the wind velocity must be around 50 km $s^{-1}$, much smaller than observed startburst-driven winds, and more importantly, much smaller than the observed velocity of the wind (roughly 800 km $s^{-1}$).

### 5.2 AGN activity time

The gas properties inferred from the best-fitting photoionization model, combined with the observed gas kinematics, suggest that the observed wind forms a continuous flow. This in turn suggests that the AGN was active for the time it took the gas to reach 17 kpc. The inferred wind dynamics can be used to put limits on the AGN activity time. We use the velocity law found earlier, $v(r) = v_0 \times r_{\rm kpc}^{-0.5}$, where $v_0$ is in the range 700–900 km $s^{-1}$, integrate between 3 and 17 kpc (the regions where the wind obeys the continuity equation), and obtained an AGN activity time of ∼60 Myr. This value is a lower limit, since the AGN could have been active for longer time without launching a wind during the first part of the activity phase. In addition, the wind may exist at further distances beyond 17 kpc but is too ionized and/or with a too-low density to be detected with KCWI.

An activity time of about 60 Myr is in the general range considered in other estimates that range from about $10^6$–$10^8$ yr (see e.g. Haiman & Hui 2001; Martini & Weinberg 2001). It is much longer than the AGN flickering time-scale, of order $10^5$ yr, suggested by several theoretical and observational studies (see e.g. Schawinski et al. 2015; Oppenheimer et al. 2018, and discussion by Sartori et al. 2018). Given this, we infer that the AGN became active about 150 Myr after the end of the starburst. We cannot examine the possibility of an earlier, perhaps similar AGN activity phase prior to the one considered here.

Perhaps the most intriguing aspect is the constant mass outflow rate over ∼60 Myr. This would require an original mass reservoir close to the edge of the galaxy, at about 3 kpc, which is being expelled by the AGN with basically a constant rate. More realistic scenarios would require mass outflow rates that are decreasing with time, at least for an AGN whose luminosity is roughly constant over this period. This topic is beyond the scope of this paper.

### 5.3 Infrared emission, UV absorption, and the fate of the system

Our photoionization model of the dusty gas in the gas cone suggests a massive gas component outside the primary galaxy. As long as the AGN remains active, this component should be observed through mid-infrared dust emission. According to our best-fitting photoionization model, the dust temperature ranges from 40–70 K at 1 kpc, to 10–20 K at 15 kpc, depending on the specific grain composition. The spectrum of this dust shows prominent mid-infrared emission, with a broad peak around 50μm. This peak emission is between the typical torus emission which peaks at 5–30 μm and SF heated dust with a peak around 70–100 μm. Contrary to the dust in the torus, the infrared emission from the gas cone is expected to be spatially resolved.

The optical emission lines observed by the KCWI trace a specific gas phase of the wind, with a temperature in the range $10^4$–$10^{4.5}$ K. A hotter gas component, with a temperature of $10^5$–$10^{5.5}$ K can be traced by UV absorption lines, using background objects as continuum sources. Indeed, Tripp et al. (2011) used the COS instrument on the *Hubble Space Telescope* and found 'hot-warm' plasma at $10^{5.5}$ K, traced by various UV absorption lines, at a projected distance of 68 kpc from a post-starburst E+A galaxy. According to their modelling, this component contains 10–150 times more mass than the colder gas in a post-starburst galaxy wind. Since the ionization parameter of the gas is increasing with the distance from the galaxy, and the gas temperature is expected to rise outwards, the gas may produce observable UV absorption lines. It may also become thermally unstable and reach much higher temperatures.

Finally, we can extrapolate the gas density, inferred from the best-fitting photoionization model, and the observed gas dynamics to give a rough estimate for the fate of the system. It would take the gas about 1 Gyr to reach a distance of 150 kpc, at this stage the gas density would be $5 \times 10^{-5}$ cm$^{-3}$ and its velocity will be of order 50 km $s^{-1}$. Obviously, existing CGM can stall the wind well before it reaches 150 kpc. Regardless of the exact scenario, such a wind will contribute its mass and metals to the existing CGM.

## 6 SUMMARY AND CONCLUSIONS

This work is part of a long-term project to map and analyse AGN-driven winds at the specific evolutionary stage of post-starburst E+A galaxies. In this paper, we present new observations of SDSS J003443.68+251020.9, at $z = 0.118$. The new KCWI spatially resolved spectroscopy presented here allow us to study the gas properties of the system throughout the entire field of view. Our results can be summarized as follows:

(i) The system consists of two galaxies. The primary galaxy shows prominent Balmer absorption lines and no contribution from O- and B-type stars, suggestive of a post-starburst E+A galaxy.

(ii) We model the SFH of the primary galaxy and find a starburst that started 400 Myr ago, with a peak SFR of about 120 $M_\odot$ $yr^{-1}$, with an exponential decrease to less than 10 per cent of its initial value after 200 Myr. Currently, the system is fully quenched and



Downloaded from https://academic.oup.com/mnras/article-abstract/480/3/3993/5066189 by California Institute of Technology user on 28 November 2018

there is no ongoing SF. The system shows a bulge-dominated morphology and we estimate its stellar mass to be roughly $10^{10.8}$ $M_\odot$.

(iii) We detect two kinematic components within the primary galaxy, both of which are ionized by the active BH. The narrow component is classified as a LINER, and the broader component as a Seyfert. The narrow component is fully consistent with a typical NLR in type II AGN. The velocity dispersion of the broader component (FWHM$\sim$900 km s$^{-1}$) exceeds the escape velocity of the galaxy, which suggests a galactic-scale outflow.

(iv) The KCWI observations reveal gas that extends to distances of 17 kpc from the central galaxy, far beyond the regions in which stars are detected ($\sim$3 kpc), with a conic-shaped geometry. This gas is ionized by the central BH, and its dynamics suggest an AGN-driven outflow.

(v) We construct a self-consistent photoionization model for the three gas components (NLR, high-velocity central component, and extended gas). According to our model, the central source has a bolometric luminosity of about $10^{45}$ erg s$^{-1}$ and a hard X-ray continuum. We estimate a BH mass of $10^{8.1}$ $M_\odot$, accreting at a few percent of the Eddington luminosity.

(vi) We construct a dynamical model for the gas in the gas cone, and correct for projection effects. The velocity of the gas outside the galaxy is $v(r) = 800 \times \left(\frac{r}{1\,\mathrm{kpc}}\right)^{-0.5}$ km s$^{-1}$.

(vii) The combination of photoionization and dynamical models for the gas in the cone explains all the observed line luminosities and line profiles. Together they show that the outflow forms a continuous flow, with a constant mass outflow rate of approximately 24 $M_\odot$ yr$^{-1}$. The continuity of the flow allows us to put a limit on the activity time of the central BH, which we find to be $\sim$60 Myr.

(viii) We are able to measure the gas mass in all the components. The mass outside the galaxy, roughly $10^9$ $M_\odot$, is an order of magnitude higher than the gas mass within the galaxy (NLR, central high velocity component, and neutral component traced by dust).

(ix) The total kinetic power of the wind, measured for the central high velocity component and the gas in the cone, is roughly $0.01L_{\mathrm{bol}}$.

Our new results suggest that we are witnessing a short-lived phase, in which the AGN is successfully removing most of the gas that was in the primary galaxy. Although the current AGN episode cannot be used to determine whether the AGN have contributed to the abrupt quenching of SF in the galaxy, we find that in a single episode, the AGN is able to remove most of the gas from its host galaxy. This gas continues to expand outwards and will probably mix with the surrounding CGM after a few hundreds Myr, enriching it with the metals it carried out of the galaxy.

Post-starburst E+A galaxies offer an advantage over other galaxy samples for studying AGN-driven outflows. Since these systems are fully quenched, with no ongoing SF, one can study the observed winds in the context of pure AGN feedback, with no contributions from SNe-driven winds. Their narrow stellar age distribution, which is dominated by the short lifetime of A-type stars, allows us to put such systems on a single timeline, where time is measured as the onset (or termination) of the recent starburst, and compare various wind properties as a function of time. We are currently involved in a detailed analysis of additional post-starburst galaxies showing evidence of massive AGN-driven winds, and results will be reported in a forthcoming publication.

## ACKNOWLEDGEMENTS

We thank the anonymous referee for useful comments and suggestions. We thank B. Trakhtenbrot and D. Poznanski for useful discussions regarding the manuscript. Funding for this work was provided by the Israel Science Foundation grant 284/13. SC gratefully acknowledges support from Swiss National Science Foundation grant PP00P2-163824. The spectroscopic analysis was made using ipython (Pérez & Granger 2007). We also used the following PYTHON PACKAGE: ASTROPY.[2]

This work made use of SDSS-III[3] data. Funding for SDSS-III has been provided by the Alfred P. Sloan Foundation, the Participating Institutions, the National Science Foundation, and the U.S. Department of Energy Office of Science. SDSS-III is managed by the Astrophysical Research Consortium for the Participating Institutions of the SDSS-III Collaboration including the University of Arizona, the Brazilian Participation Group, Brookhaven National Laboratory, Carnegie Mellon University, University of Florida, the French Participation Group, the German Participation Group, Harvard University, the Instituto de Astrofisica de Canarias, the Michigan State/Notre Dame/JINA Participation Group, Johns Hopkins University, Lawrence Berkeley National Laboratory, Max Planck Institute for Astrophysics, Max Planck Institute for Extraterrestrial Physics, New Mexico State University, New York University, Ohio State University, Pennsylvania State University, University of Portsmouth, Princeton University, the Spanish Participation Group, University of Tokyo, University of Utah, Vanderbilt University, University of Virginia, University of Washington, and Yale University. The data presented herein were obtained at the WMKO, which is operated as a scientific partnership among the California Institute of Technology, the University of California and the National Aeronautics and Space Administration. The Observatory was made possible by the generous financial support of the W.M. Keck Foundation.

## REFERENCES

Agnello A., Evans N. W., Romanowsky A. J., 2014, MNRAS, 442, 3284
Alatalo K. et al., 2016a, ApJS, 224, 38
Alatalo K. et al., 2016b, ApJ, 827, 106
Arav N., Borguet B., Chamberlain C., Edmonds D., Danforth C., 2013, MNRAS, 436, 3286
Baldwin J. A., Phillips M. M., Terlevich R., 1981, PASP, 93, 5
Baron D., Poznanski D., 2017, MNRAS, 465, 4530
Baron D., Stern J., Poznanski D., Netzer H., 2016, ApJ, 832, 8
Baron D., Netzer H., Poznanski D., Prochaska J. X., Förster Schreiber N. M., 2017, MNRAS, 470, 1687
Benson A. J., Bower R. G., Frenk C. S., Lacey C. G., Baugh C. M., Cole S., 2003, ApJ, 599, 38
Blustin A. J. et al., 2003, A&A, 403, 481
Bressan A., Poggianti B., Franceschini A., 2001, in Márquez I., Masegosa J., del Olmo A., Lara L., García E., Molina J., eds., QSO Hosts and Their Environments, Proc. Workshop. Kluwer Academic/ Plenum Publishers, Dordrecht, p. 171
Cai Z. et al., 2017, ApJ, 837, 71
Cales S. L., Brotherton M. S., 2015, MNRAS, 449, 2374
Cales S. L. et al., 2011, ApJ, 741, 106
Cales S. L. et al., 2013, ApJ, 762, 90
Calzetti D., Armus L., Bohlin R. C., Kinney A. L., Koornneef J., Storchi-Bergmann T., 2000, ApJ, 533, 682
Canalizo G., Stockton A., Brotherton M. S., van Breugel W., 2000, AJ, 119, 59
Cano-Díaz M., Maiolino R., Marconi A., Netzer H., Shemmer O., Cresci G., 2012, A&A, 537, L8
Cappellari M., 2012, Astrophysics Source Code Library, record ascl, ascl:1210.002

[2] www.astropy.org/
[3] www.sdss3.org

Downloaded from https://academic.oup.com/mnras/article-abstract/480/3/3993/5066189 by California Institute of Technology user on 28 November 2018

Cappellari M., Emsellem E., 2004, PASP, 116, 138
Cardelli J. A., Clayton G. C., Mathis J. S., 1989, ApJ, 345, 245
Cheung E. et al., 2016, Nature, 533, 504
Cicone C. et al., 2014, A&A, 562, A21
Cicone C., Maiolino R., Marconi A., 2016, A&A, 588, A41
Cid Fernandes R., Stasińska G., Schlickmann M. S., Mateus A., Vale Asari N., Schoenell W., Sodré L., 2010, MNRAS, 403, 1036
Di Matteo T., Springel V., Hernquist L., 2005, Nature, 433, 604
Dressler A., Smail I., Poggianti B. M., Butcher H., Couch W. J., Ellis R. S., Oemler A., Jr. 1999, ApJS, 122, 51
Dressler A.Oemler Jr. A., Poggianti B. M., Smail I., Trager S., Shectman S. A., Couch W. J., Ellis R. S., 2004, ApJ, 617, 867
Fabian A. C., 1999, MNRAS, 308, L39
Feldman F. R., Weedman D. W., Balzano V. A., Ramsey L. W., 1982, ApJ, 256, 427
Ferland G. J. et al., 2017, Revista Mexicana de Astronomia y Astrofisica, 53, 385
Ferrarese L., Merritt D., 2000, ApJ, 539, L9
Feruglio C., Maiolino R., Piconcelli E., Menci N., Aussel H., Lamastra A., Fiore F., 2010, A&A, 518, L155
Fiore F. et al., 2017, Astromony & Astrophysics, 601, 21, id.A143
French K. D., Yang Y., Zabludoff A., Narayanan D., Shirley Y., Walter F., Smith J.-D., Tremonti C. A., 2015, ApJ, 801, 1
García-Burillo S. et al., 2015, A&A, 580, A35
Gaspari M., Brighenti F., D'Ercole A., Melioli C., 2011, MNRAS, 415, 1549
Gebhardt K. et al., 2000, ApJ, 539, L13
Goto T., 2004, A&A, 427, 125
Goto T., 2007, MNRAS, 381, 187
Goto T. et al., 2003, PASJ, 55, 771
Greene J. E., Ho L. C., 2005, ApJ, 627, 721
Greene J. E., Zakamska N. L., Ho L. C., Barth A. J., 2011, ApJ, 732, 9
Gültekin K. et al., 2009, ApJ, 698, 198
Haiman Z., Hui L., 2001, ApJ, 547, 27
Hani M. H., Sparre M., Ellison S. L., Torrey P., Vogelsberger M., 2018, MNRAS, 475, 1160
Harrison C. M., Alexander D. M., Mullaney J. R., Swinbank A. M., 2014, MNRAS, 441, 3306
Heckman T. M., Best P. N., 2014, ARA&A, 52, 589
Heckman T. M., Thompson T. A., 2017, preprint (arXiv)
Heckman T. M., Miley G. K., van Breugel W. J. M., Butcher H. R., 1981, ApJ, 247, 403
Heckman T. M., Miley G. K., Green R. F., 1984, ApJ, 281, 525
Heckman T. M., Kauffmann G., Brinchmann J., Charlot S., Tremonti C., White S. D. M., 2004, ApJ, 613, 109
Heckman T., Borthakur S., Wild V., Schiminovich D., Bordoloi R., 2017, ApJ, 846, 151
Hopkins P. F., Hernquist L., Cox T. J., Di Matteo T., Robertson B., Springel V., 2006, ApJS, 163, 1
Kauffmann G. et al., 2003a, MNRAS, 346, 1055
Kauffmann G. et al., 2003b, MNRAS, 341, 33
Kaviraj S., Kirkby L. A., Silk J., Sarzi M., 2007, MNRAS, 382, 960
Kewley L. J., Dopita M. A., Sutherland R. S., Heisler C. A., Trevena J., 2001, ApJ, 556, 121
Kewley L. J., Groves B., Kauffmann G., Heckman T., 2006, MNRAS, 372, 961
King A., 2003, ApJ, 596, L27
Kormendy J., Ho L. C., 2013, ARA&A, 51, 511
Li Y.-P. et al., 2018, preprint (arXiv)
Liu C. T., Green R. F., 1996, ApJ, 458, L63
Liu G., Zakamska N. L., Greene J. E., Nesvadba N. P. H., Liu X., 2013a, MNRAS, 430, 2327
Liu G., Zakamska N. L., Greene J. E., Nesvadba N. P. H., Liu X., 2013b, MNRAS, 436, 2576
Martin C., Moore A., Morrissey P., Matuszewski M., Rahman S., Adkins S., Epps H., 2010, in Proc. SPIE, Vol. 7735, Ground-based and Airborne Instrumentation for Astronomy III, SPIE, Bellingham, p. 77350
Martini P., Weinberg D. H., 2001, ApJ, 547, 12
Moe M., Arav N., Bautista M. A., Korista K. T., 2009, ApJ, 706, 525
Morrissey P. et al., 2012, in Proc. SPIE, Vol. 8446, Ground-based and Airborne Instrumentation for Astronomy IV. SPIE, Bellingham, p. 844613
Morrissey P. et al., 2018, preprint (arXiv)
Mullaney J. R., Alexander D. M., Fine S., Goulding A. D., Harrison C. M., Hickox R. C., 2013, MNRAS, 433, 622
Nesvadba N. P. H., Lehnert M. D., Eisenhauer F., Gilbert A., Tecza M., Abuter R., 2006, ApJ, 650, 693
Netzer H., 2009, MNRAS, 399, 1907
Norton S. A., Gebhardt K., Zabludoff A. I., Zaritsky D., 2001, ApJ, 557, 150
Oppenheimer B. D., Segers M., Schaye J., Richings A. J., Crain R. A., 2018, MNRAS, 474, 4740
Osterbrock D. E., Ferland G. J., 2006, Astrophysics of Gaseous Nebulae and Active Galactic Nuclei. University Science Books, Sausalito, CA
Pérez F., Granger B. E., 2007, Comput. Sci. Eng., 9, 21
Poggianti B. M., Wu H., 2000, ApJ, 529, 157
Poggianti B. M. et al., 1999, ApJ, 518, 576
Pović M., Márquez I., Netzer H., Masegosa J., Nordon R., Pérez E., Schoenell W., 2016, MNRAS, 462, 2878
Reeves J. N., O'Brien P. T., Ward M. J., 2003, ApJ, 593, L65
Rodríguez Zaurín J., Tadhunter C. N., Rose M., Holt J., 2013, MNRAS, 432, 138
Rosario D. J., Shields G. A., Taylor G. B., Salviander S., Smith K. L., 2010, ApJ, 716, 131
Rowlands K., Wild V., Nesvadba N., Sibthorpe B., Mortier A., Lehnert M., da Cunha E., 2015, MNRAS, 448, 258
Rupke D. S. N., Veilleux S., 2013, ApJ, 768, 75
Rupke D. S., Veilleux S., Sanders D. B., 2005, ApJ, 632, 751
Rupke D. S. N., Gültekin K., Veilleux S., 2017, ApJ, 850, 40
Sartori L. F., Schawinski K., Trakhtenbrot B., Caplar N., Treister E., Koss M. J., Urry C. M., Zhang C., 2018, preprint (arXiv)
Schawinski K., Koss M., Berney S., Sartori L. F., 2015, MNRAS, 451, 2517
Sijacki D., Springel V., Haehnelt M. G., 2011, MNRAS, 414, 3656
Silk J., Rees M. J., 1998, A&A, 331, L1
Soto K. T., Martin C. L., Prescott M. K. M., Armus L., 2012, ApJ, 757, 86
Spoon H. W. W. et al., 2013, ApJ, 775, 127
Springel V. et al., 2005, Nature, 435, 629
Springel V., Di Matteo T., Hernquist L., 2005, MNRAS, 361, 776
Sun A.-L., Greene J. E., Zakamska N. L., Nesvadba N. P. H., 2014, ApJ, 790, 160
Sun A.-L. et al., 2018, preprint (arXiv)
Tombesi F., Cappi M., Reeves J. N., Palumbo G. G. C., Yaqoob T., Braito V., Dadina M., 2010, A&A, 521, A57
Tremaine S. et al., 2002, ApJ, 574, 740
Tremonti C. A., Moustakas J., Diamond-Stanic A. M., 2007, ApJ, 663, L77
Tripp T. M. et al., 2011, Science, 334, 952
Vazdekis A., Sánchez-Blázquez P., Falcón-Barroso J., Cenarro A. J., Beasley M. A., Cardiel N., Gorgas J., Peletier R. F., 2010, MNRAS, 404, 1639
Veilleux S., Osterbrock D. E., 1987, ApJS, 63, 295
Veilleux S. et al., 2013, ApJ, 776, 27
Wild V., Walcher C. J., Johansson P. H., Tresse L., Charlot S., Pollo A., Le Fèvre O., de Ravel L., 2009, MNRAS, 395, 144
Wild V., Heckman T., Charlot S., 2010, MNRAS, 405, 933
Wild V., Almaini O., Dunlop J., Simpson C., Rowlands K., Bowler R., Maltby D., McLure R., 2016, MNRAS, 463, 832
Yang Y., Zabludoff A. I., Zaritsky D., Lauer T. R., Mihos J. C., 2004, ApJ, 607, 258
Yang Y., Tremonti C. A., Zabludoff A. I., Zaritsky D., 2006, ApJ, 646, L33
Yesuf H. M., Faber S. M., Trump J. R., Koo D. C., Fang J. J., Liu F. S., Wild V., Hayward C. C., 2014, ApJ, 792, 84
Yesuf H. M., Faber S. M., Koo D. C., Lee L. L., 2017, preprint (arXiv)
York D. G. et al., 2000, AJ, 120, 1579
Zakamska N. L. et al., 2016, MNRAS, 459, 3144

Downloaded from https://academic.oup.com/mnras/article-abstract/480/3/3993/5066189 by California Institute of Technology user on 28 November 2018

## APPENDIX A: SPECTRAL FITTING

### A1 Global spectral fitting

We refer to the SDSS spectrum of the primary galaxy as the global spectrum. We subtract the best-fitting stellar model from the global spectrum and obtain the emission-line spectrum. We show six parts of this spectrum in Fig. A1: [O III] λλ 4959,5007Å, Hα λ 6563Å and [NII] λλ 6548,6584Å, [O II] λλ 3725,3727Å and Hβ λ 4861Å, and [O I] λλ 6300,6363Å and [S II] λλ 6717,6731Å (hereafter [O III], Hα, [N II], [O II], Hβ, [O I], and [S II]). The Balmer lines and the forbidden line profiles show narrow as well as broad components.

We model each emission line as a sum of two Gaussians – one which represents the narrow component and one that represents the broader component. We perform a joint fit to all the emission lines under several constrains: (1) we force the intensity ratio of the emission lines [O III] λλ 4959,5007Å and [N II] λλ 6548,6584Å to the theoretical ratio of 3:1, (2) we tie the central wavelengths of all the narrow lines so that the gas has the same systematic velocity, we do the same for the broader lines, and (3) we force the widths of all the narrow lines to show the same velocity dispersion, and we do the same for the broader lines. We show in Fig. A1 the best-fitting profiles, where we mark the narrow lines with green, the broader lines with blue, and the full fit with pink.

Using the best-fitting model, we derive the kinematic properties of the emitting gas. The FWHM velocity of the narrow lines is 320 km $s^{-1}$, and the width of the broad lines is 980 km $s^{-1}$. The narrow and broad components show roughly the same systematic velocity, and both are blueshifted by about 90 km $s^{-1}$ from the systematic redshift of the galaxy which we measure from the stellar Balmer absorption lines. Following the same arguments and analysis used in Baron et al. (2017, see Section 3.3.2 there), we find that the velocity dispersion of the broader component exceeds the escape velocity from the galaxy, even under the assumption that the gas mass is half of the stellar mass in that system.

Table A1 gives line intensities, reddening corrected line luminosities, and derived fit parameters for all measured emission lines. The uncertainties of the widths and central wavelengths are obtained from the $\chi^2$ minimization process, and are tied to each other as discussed above. We propagate these uncertainties and the uncertainties on the dust reddening to calculate the uncertainties in line intensity and extinction corrected luminosity.

### A2 Spatially resolved spectral fitting

To increase the S/N of the spatially resolved spectra, we divide the spaxels into bins with similar distance from the primary galaxy using shells, as described in Section 3.3.2. We show in Fig. A2 the spaxels that were used in the different shells, where each colour corresponds to a single shell. In Fig. A3, we show the Hβ and Hγ emission-line regions of the binned spectra, as a function of distance from the primary galaxy. In order to reduce the uncertainty in fitting the Hγ line, we fit simultaneously the Hβ and Hγ lines with a single Gaussian for each, tying their central wavelengths and velocity dispersions. The best-fitting profiles are marked with red in Fig. A3.

Since the He II emission line is even weaker than the Hγ, we bin the spectra into four, rather than eight, bins, as a function of distance from the primary galaxy. For each bin, we fit simultaneously the Hβ and the He II lines, which we model with a single Gaussian, and we tie their central wavelengths and velocity dispersions. We show the stacked spectra, centred around the Hβ emission line in the top panels of Fig. A4, and around the He II emission line in the bottom panels of the figure. The best-fitting profiles are marked with red.

We list in Table A2, the luminosities of the lines measured in eight shells and the dust reddening calculated from the Hβ/Hγ ratio. In Table A3, we list the He II and Hβ luminosities measured in four shells. Finally, Table A4 lists the W80 values measured for the [O III] emission line as a function of distance from the central galaxy.

Downloaded from https://academic.oup.com/mnras/article-abstract/480/3/3993/5066189 by California Institute of Technology user on 28 November 2018

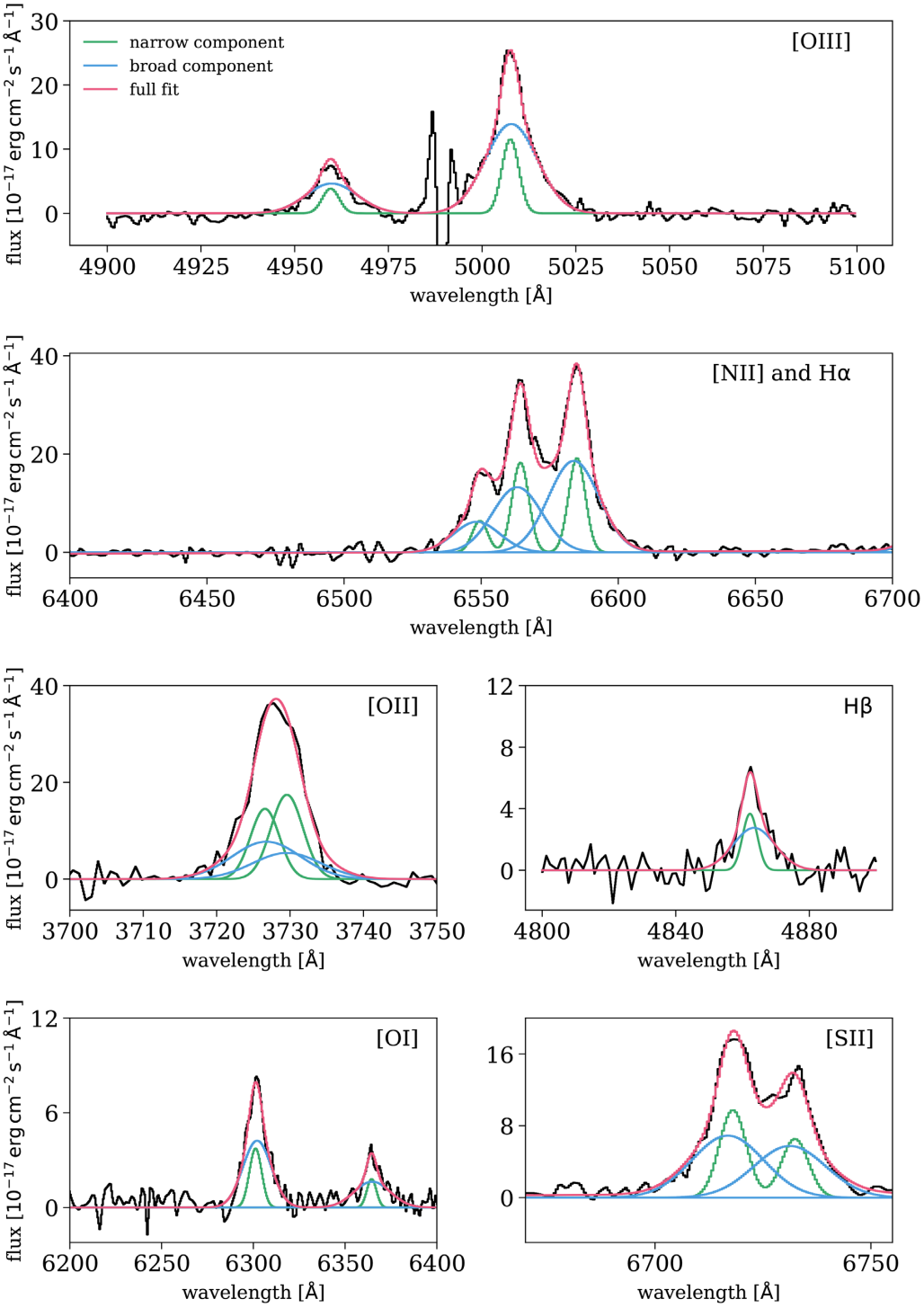


**Figure A1.** The emission-line spectrum (black) of the gas in the galaxy as obtained by subtracting the best-fitting population synthesis model from the global (SDSS) spectrum. We show [O III], H$\alpha$ and [N II], [O II], H$\beta$, [O I], and [S II] as indicated on each panel. We use two Gaussians to account for the narrow and broad components, and plot these in green (narrow lines) and blue (broad lines). The full fit is plotted in pink.

Downloaded from https://academic.oup.com/mnras/article-abstract/480/3/3993/5066189 by California Institute of Technology user on 28 November 2018

**Table A1.** Best-fitting model parameters for the two Gaussian fit. The best-fitting intensities are normalized with respect to the median value of the entire spectrum. The central wavelengths and widths of the Gaussians are tied together for a given velocity component. The luminosities are corrected for reddening by foreground ISM-type dust assuming H$\alpha$/H$\beta$=2.85. Vacuum wavelength are used relative to the systemic velocity obtained from the stellar absorption lines in the primary galaxy.

| Emission line | Intensity ($10^{-17}$ erg s$^{-1}$ cm$^{-2}$) | Luminosity (erg s$^{-1}$) |
|---|---|---|
| Narrow lines: $\sigma = 135 \pm 20$ km s$^{-1}$, WL([O III]$\lambda$5008.24) $= 5006.6 \pm 0.2$Å | | |
| H$\beta$ | $30.7 \pm 2.9$ | $4.96 \pm 0.51 \times 10^{40}$ |
| [O III]$\lambda$4959 | $21.6 \pm 2.3$ | $3.62 \pm 0.38 \times 10^{40}$ |
| [O III]$\lambda$5007 | $65.4 \pm 5.0$ | $10.75 \pm 0.82 \times 10^{40}$ |
| [O I]$\lambda$6300 | $31.4 \pm 5.6$ | $3.39 \pm 0.61 \times 10^{40}$ |
| [N II]$\lambda$6548 | $45.7 \pm 3.5$ | $4.63 \pm 0.35 \times 10^{40}$ |
| H$\alpha$ | $140.0 \pm 11.1$ | $14.2 \pm 1.1 \times 10^{40}$ |
| [N II]$\lambda$6584 | $147.4 \pm 10.8$ | $14.8 \pm 1.1 \times 10^{40}$ |
| [S II]$\lambda$6717 | $110.8 \pm 7.9$ | $10.81 \pm 0.95 \times 10^{40}$ |
| [S II]$\lambda$6731 | $80.1 \pm 6.34$ | $7.79 \pm 0.88 \times 10^{40}$ |
| Blueshifted broad lines: $\sigma = 416 \pm 70$ km s$^{-1}$, WL([O III]$\lambda$5008.24) $= 5006.9 \pm 1.4$Å | | |
| H$\beta$ | $19.1 \pm 3.1$ | $21.2 \pm 3.4 \times 10^{41}$ |
| [O III]$\lambda$4959 | $79.9 \pm 5.6$ | $71.8 \pm 5.3 \times 10^{41}$ |
| [O III]$\lambda$5007 | $242.1 \pm 9.7$ | $213.2 \pm 8.5 \times 10^{41}$ |
| [O I]$\lambda$6300 | $82 \pm 12$ | $15.6 \pm 2.2 \times 10^{41}$ |
| [N II]$\lambda$6548 | $143.3 \pm 5.1$ | $21.2 \pm 0.77 \times 10^{41}$ |
| H$\alpha$ | $298 \pm 13$ | $60.0 \pm 2.1 \times 10^{41}$ |
| [N II]$\lambda$6584 | $430 \pm 15$ | $63.7 \pm 2.2 \times 10^{41}$ |
| [S II]$\lambda$6717 | $125.4 \pm 6.4$ | $16.6 \pm 1.3 \times 10^{41}$ |
| [S II]$\lambda$6731 | $91.3 \pm 5.8$ | $12.0 \pm 1.2 \times 10^{41}$ |

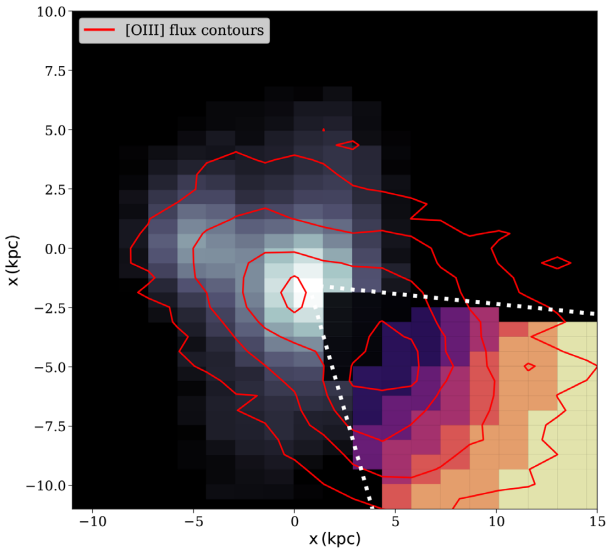


**Figure A2.** The seven shells referred to in the text and listed in Table A2. The region of the primary galaxy is not marked in this figure. The background colour represents the stellar continuum emission, and the red contours represent [O III] flux in logarithmic scale. The shells are defined between the two dashed white lines. We colour spaxels that correspond to a given shell with the same colour.

Downloaded from https://academic.oup.com/mnras/article-abstract/480/3/3993/5066189 by California Institute of Technology user on 28 November 2018

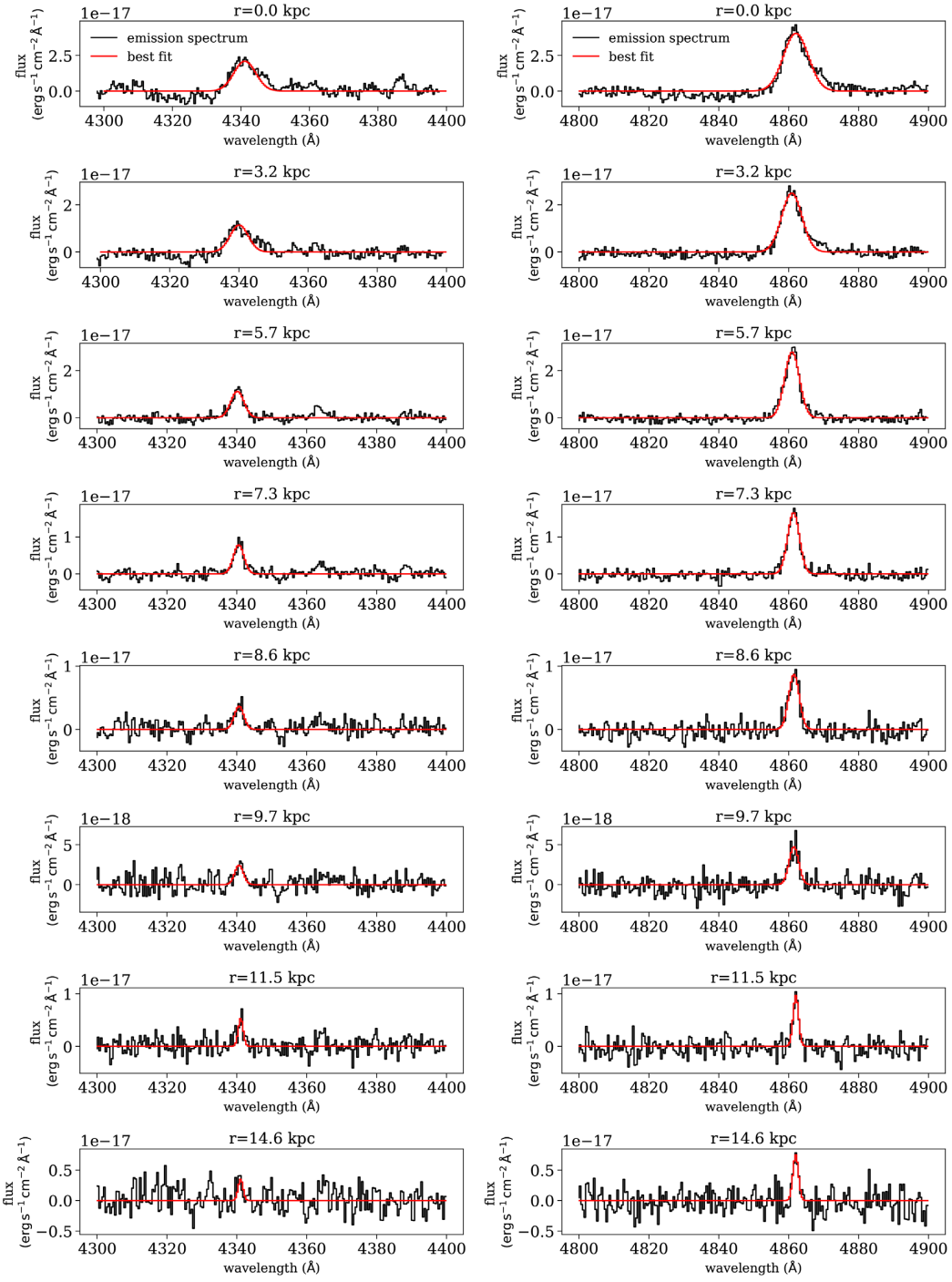


**Figure A3.** Stacked emission-line spectra as a function of distance from the primary galaxy, where the left-hand panels show the H$\gamma$ region and the right-hand panels show the H$\beta$ region (black). Inside the primary galaxy (distances smaller than 3 kpc), we subtract the stellar continuum before stacking. The best-fitting profiles are marked with red.

Downloaded from https://academic.oup.com/mnras/article-abstract/480/3/3993/5066189 by California Institute of Technology user on 28 November 2018

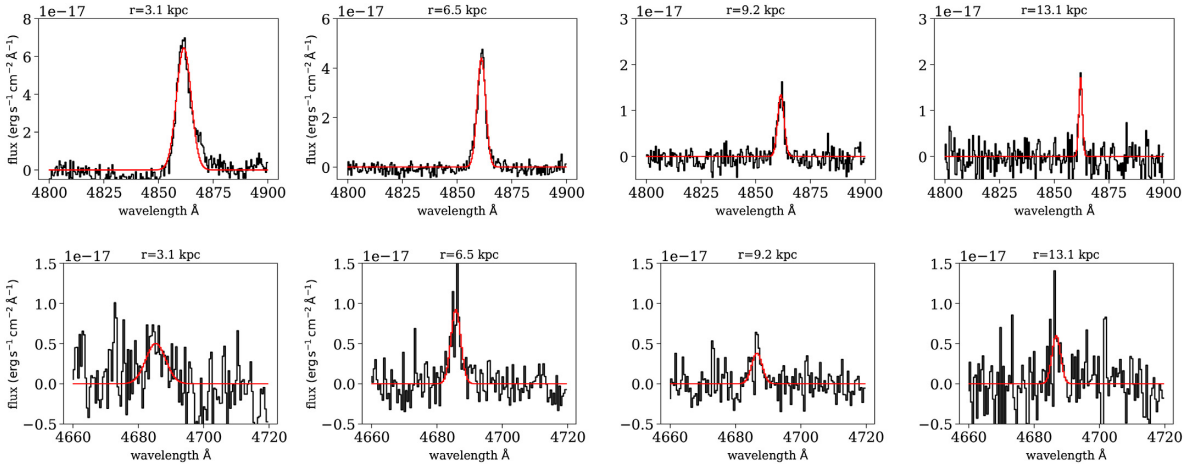


**Figure A4.** Stacked spectra along the gas cone, as a function of distance from the primary galaxy. The upper panels show the H$\beta$ emission-line region and the lower panels show the He II emission-line region. The best-fitting profiles are marked with red.

**Table A2.** Spatially resolved emission-line measurements for the eight different shells. The first measurement corresponds to the primary galaxy, where we sum 3 × 6 spaxels around the central source, which corresponds to 2 arcsec×4.1 arcsec. We designate this range (which is not spherical) as 'primary'. The next seven measurements correspond to the different shells. Uncertainties on distance are given as the standard deviation of distances of the spaxels from the central source. The listed luminosities are not reddening corrected since this depends on the assumed dust geometry (see Section 4.3).

| Distance (kpc) | [O III] luminosity ($10^{40}$ erg s$^{-1}$) | H$\beta$ luminosity ($10^{39}$ erg s$^{-1}$) | H$\gamma$ luminosity ($10^{39}$ erg s$^{-1}$) | $E(B-V)$ (mag) |
|---|---|---|---|---|
| 'Primary' | $4.63 \pm 0.58$ | $9.2 \pm 1.3$ | $3.33 \pm 0.57$ | $0.531 \pm 0.066$ |
| $3.1 \pm 1.5$ | $3.35 \pm 0.25$ | $4.63 \pm 0.40$ | $1.75 \pm 0.17$ | $0.438 \pm 0.076$ |
| $5.72 \pm 0.94$ | $3.34 \pm 0.11$ | $3.76 \pm 0.14$ | $1.541 \pm 0.072$ | $0.281 \pm 0.085$ |
| $7.34 \pm 0.54$ | $1.954 \pm 0.093$ | $1.798 \pm 0.095$ | $0.753 \pm 0.050$ | $0.234 \pm 0.081$ |
| $8.62 \pm 0.62$ | $1.021 \pm 0.059$ | $0.841 \pm 0.056$ | $0.357 \pm 0.030$ | $0.195 \pm 0.079$ |
| $9.72 \pm 0.53$ | $0.566 \pm 0.076$ | $0.419 \pm 0.064$ | $0.194 \pm 0.035$ | $0.05 \pm 0.10$ |
| $11.5 \pm 1.13$ | $0.53 \pm 0.10$ | $0.48 \pm 0.10$ | $0.228 \pm 0.064$ | $0.00 \pm 0.10$ |
| $14.6 \pm 1.75$ | $0.37 \pm 0.14$ | $0.38 \pm 0.16$ | $0.178 \pm 0.098$ | $0.00 \pm 0.13$ |

Downloaded from https://academic.oup.com/mnras/article-abstract/480/3/3993/5066189 by California Institute of Technology user on 28 November 2018

**Table A3.** Spatially resolved emission-line measurements for the four different shells. The luminosities we list are not corrected for dust, since they depend on the assumed dust geometry (see Section 4.3).

| Distance (kpc) | H$\beta$ luminosity ($10^{39}$ erg s$^{-1}$) | He II luminosity ($10^{39}$ erg s$^{-1}$) |
|---|---|---|
| $2.75 \pm 1.50$ | $7.13 \pm 0.81$ | $1.74 \pm 0.49$ |
| $6.53 \pm 1.74$ | $7.02 \pm 0.92$ | $1.17 \pm 0.45$ |
| $9.17 \pm 1.20$ | $1.88 \pm 0.75$ | $0.59 \pm 0.23$ |
| $13.0 \pm 3.51$ | $1.31 \pm 0.41$ | $0.77 \pm 0.29$ |

**Table A4.** $W_{80}$([O III]) as a function of distance from the centre of the primary galaxy. $W_{80}$ is defined as the width of the [O III] that contains 80 percent of its integrated flux: $W_{80} = v_{90} - v_{10}$, where $v_{10}$ and $v_{90}$ are the velocities that correspond to the 10th and 90th percentiles of the integrated [O III] flux. The uncertainties on the distance represent the different shells we used, and the uncertainties on W80 represent the 85th and 75th percentiles of the flux.

| Distance (kpc) | W80 (km s$^{-1}$) |
|---|---|
| 'Primary' | $1040^{+215}_{-130}$ |
| $1.57^{+0.65}_{-0.78}$ | $1013^{+245}_{-133}$ |
| $2.87^{+0.27}_{-0.65}$ | $720^{+191}_{-92}$ |
| $3.42^{+0.51}_{-0.27}$ | $538^{+147}_{-75}$ |
| $4.45^{+0.69}_{-0.51}$ | $292^{+41}_{-23}$ |
| $5.83^{+0.51}_{-0.69}$ | $240^{+36}_{-20}$ |
| $6.87^{+0.38}_{-0.51}$ | $219^{+24}_{-15}$ |
| $7.64^{+0.45}_{-0.38}$ | $208^{+28}_{-15}$ |
| $8.56^{+0.31}_{-0.45}$ | $206^{+24}_{-14}$ |
| $9.19^{+0.39}_{-0.31}$ | $192^{+31}_{-17}$ |
| $9.98^{+0.76}_{-0.39}$ | $185^{+34}_{-15}$ |
| $11.5^{+1.5}_{-0.76}$ | $172^{+25}_{-11}$ |
| $14.5^{+1.5}_{-1.5}$ | $110^{+16}_{-11}$ |

This paper has been typeset from a TEX/LATEX file prepared by the author.

Downloaded from https://academic.oup.com/mnras/article-abstract/480/3/3993/5066189 by California Institute of Technology user on 28 November 2018